International Journal of Engineering Science 226 (2026) 104573

Contents lists available at ScienceDirect

International Journal of Engineering Science

journal homepage: www.elsevier.com/locate/ijengsci

Enhanced energy harvesting potential of inertially amplified nonlinear piezomagnetoelastic chains☆

A. Bhattacharyya *,[1], S. Adhikari

James Watt School of Engineering, The University of Glasgow, Glasgow G12 8QQ, UK

ARTICLE INFO

Keywords:
Vibration energy harvesting
Nonlinear metamaterials
Transient free waves
Harmonic balance method
Evanescent bloch waves

ABSTRACT

Conventional vibration energy harvesters are commonly designed around sustained external excitation and narrow resonance tuning, which can limit performance when disturbances are intermittent and energy is carried by transient free wave motion. To address this limitation, we propose a framework for vibration energy harvesting from transient free waves in an inertially amplified, nonlinear, periodic piezomagnetoelastic chain. A reduced electromechanical model is developed to characterize free wave propagation and energy conversion in both the linearized and strongly nonlinear regimes. No external forcing or excitation is applied to the system and the harvesting potential is characterized in the regime of free wave propagation generated solely by initial conditions imposed on the tip mass. An analytical approach is developed to predict the maximum steady-state harvested power and the associated free-wave operating frequency directly from the coupled structural, magnetic, inertial, and electrical parameters of the system, and is validated against numerical time-domain simulations. The results show that magnetic bi-stability and inertial amplification can fundamentally reshape the harvesting landscape. Whereas in the linearized regime, the system exhibits a sharply tuned optimum, the strongly nonlinear regime produces a broad quasi-saturated band of near optimal performance over a much wider range of free wave frequencies. This broadening is achieved within stable intrawell oscillations, without relying on negative-stiffness induced divergence, and enables high harvesting performance to be maintained with an improved stiffness-to-weight ratio through stiffer coupling and lower auxiliary inertia. These findings show that the enhanced harvesting potential of nonlinear inertially amplified piezomagnetoelastic chains lies in broadening and stabilizing the high-performance operating regime, rather than merely increasing a single-frequency peak, thereby providing a robust and physically realizable route for harvesting energy from transient free waves.

Nomenclature

See Table 1.

☆ A. Bhattacharyya acknowledges the James Watt School of Engineering Ph.D. scholarship received from the University of Glasgow.

* Corresponding author.
E-mail address: 2756762b@student.gla.ac.uk (A. Bhattacharyya).
[1] Doctoral researcher.

https://doi.org/10.1016/j.ijengsci.2026.104573
Received 4 April 2026; Received in revised form 5 May 2026; Accepted 6 May 2026
Available online 22 May 2026

Table 1
Principal notations and abbreviations used in the manuscript.

Symbol	Description	Units
General notation and wave variables		
t	Time	s
$\dot{(\cdot)}$	Derivative with respect to time t	–
n	Unit-cell index in the periodic chain	–
N	Number of unit cells in the finite chain used for simulations	–
i	Imaginary unit, $i^2 = -1$	–
μ	Bloch wavenumber or phase advance per unit cell	–
$Re(\cdot)$, $Im(\cdot)$	Real and imaginary parts of a complex quantity	–
$\mathrm{sgn}(\cdot)$	Sign function	–
ω	Free-wave angular frequency	rad s^{-1}
ω_e	Optimum free-wave frequency associated with maximum harvested power	rad s^{-1}
T	Period used for averaged-power evaluation, typically $T = 2\pi/\omega$	s
Beam, piezoelectric patch, and magnetic parameters		
ρ, E	Density and Young's modulus of the beam	kg m^{-3}, GPa
L, w, h	Length, width, and thickness of the cantilever beam	mm
EI	Flexural rigidity of the beam	N m^2
L_c, w_c, h_c	Length, width, and thickness of the piezoelectric patch	mm
d_{31}	Piezoelectric strain coefficient	pC N^{-1}
C_p	Piezoelectric capacitance	nF
R_l	Load resistance	MΩ
a, $2b$	Radius and vertical length of each base magnet	mm
a_t, $2b_t$	Radius and vertical length of the tip magnet	mm
d_h, d_v	Horizontal and vertical distances defining the magnet configuration	mm
$d = 2d_h$	Separation distance between the two base magnets	mm
B_s, B_t	Magnetic field strengths at the surfaces of the base and tip magnets	T
μ_0	Magnetic permeability of free space	N A^{-2}
M_t	Tip mass attached to the cantilever beam	g
I_t/M_t	Mass-normalized rotational inertia of the tip mass	mm^2
m_t	Magnetic moment of the tip magnet	A m^2
Unit-cell electromechanical model		
$Y(t)$	Transverse displacement of the tip mass in the isolated unit cell	m
$V(t)$	Voltage generated across the piezoelectric load in the isolated unit cell	V
$Y_n(t)$	Tip-mass displacement of the nth unit cell	m
$V_n(t)$	Voltage generated in the nth unit cell	V
$q_n(t)$	Charge variable associated with the piezoelectric capacitance	C
Q	Complex amplitude of the harmonic charge response	C
γ_c	Intermediate piezoelectric coupling constant of the bimorph patch	C
Θ	Electromechanical coupling coefficient between displacement and voltage	C m^{-1}
$\tau = R_l C_p$	Electrical time constant of the resistive-capacitive circuit	s
π_M	Magnetic potential energy of the tip magnet	J
c_0, c_1, c_2	Constant, quadratic, and quartic coefficients of the magnetic potential approximation	J, N m^{-1}, N m^{-3}
Y_s	Static equilibrium position of the tip mass in the bi-stable potential	m
$U(Y_n)$	Effective potential energy of the uniform branch	J
k_{eff}	Effective linear stiffness contribution of the cantilever beam	N m^{-1}
K_t	Tangent stiffness evaluated about a stable equilibrium	N m^{-1}
Periodic chain and inertial-amplification quantities		
k	Linear coupling-spring stiffness between adjacent unit cells	N m^{-1}
m_a	Auxiliary mass used in the inertial-amplification mechanism	kg
α	Inclination angle of the inertial-amplifier links	rad
r_a	Inertial-amplification factor, $r_a = m_a \cos^2\alpha / \sin^2\alpha$	kg
$m_e(\mu)$, $m_e(\omega)$	Effective Bloch-reduced inertia of the mechanical equation	kg
$K(\mu)$, $K(\omega)$	Effective Bloch-reduced stiffness of the mechanical equation	N m^{-1}
$\chi(\omega)$	Compact notation for $\cos\mu(\omega)$ in the dispersion analysis	–
β	Evanescent attenuation parameter associated with $\lvert\Im(\mu)\rvert$	–
ω_0	Natural frequency of the homogeneous linearized mechanical equation	rad s^{-1}
State-space and eigenvalue notation		
$\mathbf{y}(t)$	State vector, typically $\mathbf{y}(t) = \{Y_n, \dot{Y}_n, V_n\}^T$	mixed
$\mathbf{y}_0$	Initial state vector	mixed
$A(\omega)$, $B(\omega)$	Coefficient matrices in the frequency-dependent state-space formulation	mixed
$S(\omega)$	Standard state matrix obtained from the coupled electromechanical equations	s^{-1}
λ_i	Eigenvalues of the state matrix $S(\omega)$	s^{-1}
v_i, w_i	Right and left eigenvectors of $S(\omega)$	mixed
c_i	Modal coefficient multiplying the ith voltage contribution	V
e_3	Unit vector used to extract the voltage component of the state vector	–
s	Laplace-domain complex variable	s^{-1}
$s_j(\omega)$	Poles of the linearized electromechanical system	s^{-1}

(*continued on next page*)

Table 1 (*continued*).

$\sigma(\omega)$	Modal decay rate used in post-transient estimates	s^{-1}
$\omega_d(\omega)$	Damped oscillation frequency of a complex-conjugate pole pair	rad s^{-1}
Harvested-power quantities		
P_{ave}	Averaged electrical power harvested over a prescribed time window	W
$P_{\max}(\omega)$	Maximum harvested power evaluated as a function of free-wave frequency	W
t_s	Settling time after which the initial transient response is sufficiently decayed	s
t_0	Starting time of the post-transient averaging window	s
$t_0^*(\omega)$	Optimized post-transient averaging-window location	s
$T_d(\omega)$	Damped or effective period used for power averaging	s
$E(t_0,\omega)$	Residual associated with stationarity of averaged power with respect to t_0	W s^{-1}
$F(t_0,\omega)$	Residual associated with stationarity of averaged power with respect to ω	W s
Nonlinear and harmonic-balance quantities		
$u_n(t)$	Intrawell displacement perturbation from a stable equilibrium, $Y_n(t) = Y_s + u_n(t)$	m
U_0	Zero-harmonic correction in the nonlinear intrawell expansion	m
A_m, B_m	Cosine and sine coefficients of the mth harmonic	m
R	First-harmonic oscillation amplitude in the nonlinear intrawell approximation	m
φ	Phase shift in the first-harmonic representation	rad
$\hat{U}_1$	Complex amplitude of the first-harmonic displacement perturbation	m
$\hat{V}_1$	Complex amplitude of the first-harmonic voltage response	V
M	Number of harmonics retained in the nonlinear harmonic expansion	–
Abbreviations		
HBM	Harmonic Balance Method	–
IBZ	Irreducible Brillouin zone	–
DOF	Degree of freedom	–
LTI	Linear time-invariant system	–

Note: A few symbols, such as a, b, A, B, c_i, and ϵ, are also used locally in intermediate algebraic derivations. Only the principal symbols needed for following the main electromechanical, dispersion, and energy-harvesting analyses are listed here.

1. Introduction

Energy harvesting from ambient motion and structural vibrations remains an attractive route for powering distributed sensors and low-power electronics in settings where wiring is impractical and battery replacement is costly. Piezoelectric transduction is particularly appealing because of its relatively high energy density, direct electromechanical conversion, and compatibility with slender structural members and beam-type architectures (Stephen, 2006; Wei & Jing, 2017; Williams & Yates, 1996). At the same time, the central limitation of classical harvesters is well known as in high output is usually obtained only in a narrow neighborhood of resonance with the frequency of external excitations, which makes performance highly sensitive to excitation frequency and to the presence of sustained external forcing (Anton & Sodano, 2007; Daqaq et al., 2014; Erturk & Inman, 2011). This has motivated a large body of work on nonlinear and multistable devices aimed at broadening the useful operating range (Cottone et al., 2009; Harne & Wang, 2013; Kim & Seok, 2014). Further extensions have explored bi-stability concepts, electrical tuning strategies, and nonlinear sinks to improve robustness away from a single resonant peak (Morel et al., 2018; Scarselli et al., 2016; Xiong et al., 2018). Nevertheless, most of this literature still treats energy harvesting as a mechanism driven by persistent harmonic or base excitation, with comparatively less attention paid to intermittent disturbances present in the surrounding vibrational environment of real-world structures that are more naturally interpreted as initial conditions launching transient wave motion. In this context, Cao et al. (2020) proposed a nonlinear electromechanical model for an axially preloaded cantilever beam where the preload helps to lower the resonant frequency so that it can match well with the frequency domain of a practical vibrational environment. But, still the model required a well-defined preload and base excitation.

Recent developments in quasi-zero stiffness and low-frequency nonlinear vibration systems further show that geometric nonlinearity, tunable stiffness, and multi-stability can be exploited to extend the effective operating range of vibration attenuation and energy conversion devices. For example, QZS-based harvesters and isolators have been shown to exhibit monostable, zero-linear stiffness, and bistable oscillation modes, as well as enhanced robustness under mass-load deviation (Meng, Hou, Lin, et al., 2025; N.A. Saeed et al., 2025). Related studies have also addressed subharmonic response suppression, broadband tunable-stiffness isolation, and nonlinear interactions in layered or bio-inspired low-frequency isolators (Meng, Hou, Wanget al., 2025; Saeed et al., 2026). In addition, nonlinear piezoelectric harvesting with RL-loads and internal-resonance effects, together with adaptive harmonic-balance formulations, has provided useful analytical tools for treating strongly nonlinear electromechanical responses (Lin et al., 2023; N. Saeed et al., 2025). X-shaped and multi-layer nonlinear isolator configurations have likewise demonstrated rich resonance interactions and low-frequency vibration-control capabilities (N.A. Saeed et al., 2025; Saeed et al., 2024). Nevertheless, these studies are primarily concerned with forced-response vibration isolation, harmonic excitation, or device-level nonlinear response optimization.

A complementary route has emerged from phononic materials, elastic metamaterials, and periodic waveguides, where the objective is not merely to tune a local resonance, but to shape how vibrational energy propagates, localizes, and attenuates before it is converted into electricity (Gonella et al., 2009; Hussein et al., 2014; Kushwaha et al., 1993). Foundational studies on band gap formation and locally resonant media established that dispersion engineering can be used to suppress, trap, or redirect elastic energy in highly structured systems (Mikoshiba et al., 2013; Yilmaz et al., 2007). Building on this foundation, wave-based harvesting

has been enhanced through acoustic mirrors, metamaterial-inspired focusing concepts, and defect-mediated localization (Carrara et al., 2012, 2013; Lv et al., 2013). More recent studies have extended this idea to tunable sub-wavelength plates, multifunctional piezoelectric metastructures, defect-coupled phononic beams, and elastic metasurfaces for enhanced energy harvesting (Geng et al., 2021; Lin & Tol, 2021; Oudich & Li, 2017; Sugino & Erturk, 2018). Collectively, these works demonstrate that spatial periodicity can substantially enhance harvesting efficiency by concentrating mechanical energy in targeted regions of a structure. However, these systems are still predominantly analyzed under sustained forcing, and their design is often guided by extensive parametric sweeps rather than by compact analytical criteria that directly connect the harvesting optimum to the coupled structural and electrical parameters.

Nonlinear bi-stability adds a further layer of richness to this problem. The classical magnetoelastic work of Moon and Holmes (Moon & Holmes, 1979), together with the general nonlinear dynamical framework summarized by Strogatz (Strogatz, 1994), established how double well oscillators can exhibit intrawell oscillations, interwell transitions, saddle crossings, and complex phase space structure. These ideas have since been translated into piezomagnetoelastic and nonlinear piezoelectric harvesters, where nonlinearity can broaden the effective operating range and alter the energy conversion pathway (Aravind Kumar et al., 2015; Friswell et al., 2012). In parallel, nonlinear periodic structures with bi-stability have revealed transition waves, solitons, amplitude-dependent dispersion, and input excitation-independent wave-guided harvesting opportunities (Hwang & Arrieta, 2022; Nadkarni et al., 2014; Raney et al., 2016). In terms of a cantilever beam with a tip mass, which is somewhat close to the unit-cell model proposed in this work, sufficient conditions for the existence of periodic oscillatory behavior has been established in the general nonlinear regime (Esmailzadeh & Nakhaie-Jazar., 1998) in the presence of harmonic base excitations. Yet the new unit-cell phase plane behavior reported in the present study makes clear that a piezomagnetoelastic cell with electrical coupling is not a conservative bi-stable oscillator, because the coupling terms continuously transfer mechanical energy into the shunt circuit and the relevant trajectories are dissipative spirals rather than closed periodic or homoclinic orbits. This observation is important because it changes the role of the unit cell when it is embedded in a periodic chain. The resulting medium is expected to support not only nonlinear confinement and transient snap-through, but also distributed attenuation and spatially extended electrical energy extraction without the need of any sustained external forcing.

The gap in the literature therefore lies at the intersection of four themes that have usually been treated separately: nonlinear bi-stability, piezoelectric transduction, transient free wave motion and inertial amplification in periodic media. Existing studies on nonlinear wave propagation and piezoelectric metastructures have clarified important mechanisms of amplitude-dependent transport and electromechanical interaction (Mosquera-Sánchez & Jr., 2021; Narisetti, 2010). Existing wave-harvesting studies have shown how band gaps, localization, and topological transport can be exploited for energy conversion (Chaplain et al., 2020; Sugino & Erturk, 2018). However, there is still no analytical framework for a nonlinear inertially amplified piezomagnetoelastic chain that starts from a dissipative bi-stable unit cell, treats the excitation as transient free wave motion generated solely by initial conditions, and then predicts the operating regime for maximum steady-state harvested power directly from the coupled magnetic, inertial, structural, and electrical parameters. This is precisely the problem addressed here, and it is scientifically important because real engineered systems are often subjected to intermittent disturbances rather than idealized persistent forcing and proposes a design framework that can exploit such free wave motion which would therefore be both more general and more practically relevant.

The methodological novelty of the present work is twofold. First, a reduced electromechanical model is developed for an inertially amplified nonlinear piezomagnetoelastic chain and analyzed in both the linearized intrawell regime and the strongly nonlinear intrawell regime. In the linearized regime, Bloch reduction is combined with a settling-time-aware power criterion to obtain a predictive analytical framework for the maximum steady-state harvested power and its associated free-wave operating frequency. Second, the analysis is extended to the nonlinear regime through an amplitude-dependent dispersion relation and direct time-domain power evaluation, allowing the role of magnetic bi-stability and inertial amplification to be assessed beyond the sharply tuned linearized optimum. The novelty of the results is equally significant. Rather than merely increasing a single harvesting peak, the strongly nonlinear regime is shown to generate a broad quasi-saturated band of near optimal performance over a much wider free wave frequency interval, while remaining within stable intrawell oscillations and avoiding negative-stiffness induced divergence. In the present design, this broadened operating window is obtained simultaneously with an improved stiffness-to-weight ratio through stiffer coupling and reduced auxiliary inertia, which is especially attractive from the perspective of real structural design. The broader impact of this work is therefore to reposition transient free wave motion in nonlinear periodic electromechanical media as a deliberate design resource for robust, distributed, and physically realizable energy harvesting, rather than as a transient precursor to a conventionally forced steady state.

2. A piezomagnetoelastic unit-cell model

As a repeating unit-cell model for our periodic structure, we consider a vertical cantilever Euler–Bernoulli beam with uniform cross-section of length L, width w and thickness h with a tip mass M_t and a piezoelectric patch at the base near the fixed end. The tip mass is subject to a magnetic field created by two repelling permanent magnets located symmetrically with the north pole facing upwards, on either side of the clamped position of the beam. The tip mass is considered to be significantly larger than the mass of the beam. A schematic diagram of the beam-mass-magnet unit cell is shown in Fig. 1 with the dimensions labeled. Each of the two permanent magnets is considered to have a radius a in the horizontal direction and length $2b$ in the vertical direction. The vertical distance between the center of the tip mass and the center of base magnets is denoted as d_v and the horizontal distance between the center of the tip mass and the center of either magnet is denoted as d_h. Piezoelectric patches are pasted in a bimorph 31 configuration near the fixed end of each beam in the chain for electrical energy harvesting from free wave motion through the chain. The beam material is considered to be isotropic with density ρ.

We make the following assumptions for our system without loss of generality for our present objective:

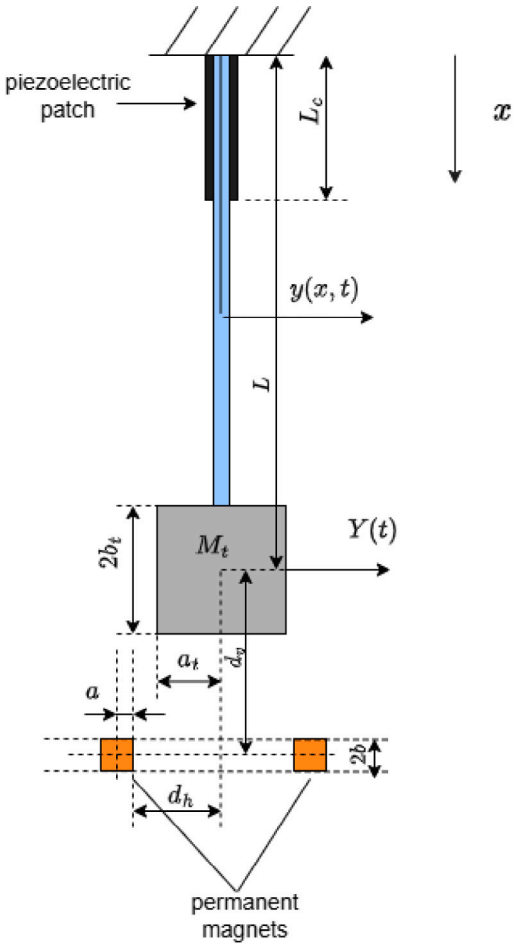

Fig. 1. The repeating piezomagnetoelastic unit-cell model.

1. The magnetic forces acting on the tip mass are considered to be derived from a potential function represented by a fourth order polynomial which is a reasonable truncation of the Moon-Holmes model (Moon & Holmes, 1979) and will be justified later in this Section.
2. The mass of the beam is considered to be negligible when compared to the tip mass.
3. We use a single-mode approximation for the general transverse displacement of the beam and neglect the contribution from higher modes of vibration again without loss of generality for our present objective.

The axial displacement of the beam and hence the tip mass are considered to be negligible in comparison to the transverse displacement. Since the mass of the beam is considered to be negligible when compared to the tip mass, the beam is considered as a purely flexural element with flexural rigidity EI and the kinetic energy of the system arises only due to the tip mass. For the same reason, the general transverse displacement at any point in the beam can be expressed in terms of the tip mass displacement using a relationship based on the first mode of the linear mode shape of the beam. Essentially, we use a single mode approximation for the beam displacement neglecting the contribution from higher modes of vibration.

The magnetic potential energy is considered in accordance to the Moon and Holmes model (Moon & Holmes, 1979) where it has been considered to be a sixth order polynomial in terms of the beam tip displacement as:

$$\pi_M = c_0 + c_1 Y^2 + c_2 Y^4 + c3Y^6 \tag{1}$$

where c_0, c_1, c_2, c_3 are constant coefficients dependent on the magnetic parameters of the system. This magnetic potential energy function can be studied to find its stationary points or in other words the fixed points of the system where the nonlinearities arise solely due to the external magnets and the dependence of those fixed points on the system parameters to characterize the different types of system bifurcations (Aravind Kumar et al., 2015). Since the present objective is to capture the leading order physics of free intrawell wave propagation and energy harvesting in a symmetric bi-stable regime, we adopt a fourth-order truncation of the Moon–Holmes magnetic potential. This is the lowest order polynomial that preserves the qualitative phase-space topology relevant

to the analysis, namely two stable equilibria separated by an unstable saddle, and therefore retains the essential ingredients for barrier crossing, intrawell dynamics, and localized electromechanical energy conversion. In this sense, the quartic potential is used here as a normal-form representation of the magnetic nonlinearity over the dynamically relevant displacement range explored by the transient wave. The neglected sixth-order contribution is expected mainly to modify the far-from-equilibrium stiffness and the quantitative well depth at larger amplitudes, rather than the existence of the bi-stable landscape itself. Accordingly, the fourth-order truncation is most appropriate for trajectories that explore a single potential well without relying on extreme far-field excursions. We therefore emphasize that the quartic model is not intended as an exact global reconstruction of the full magnetostatic interaction, but as a controlled reduced model for the qualitative intrawell-wave and harvesting mechanisms studied here. Inclusion of the sixth-order coefficient might be quantitatively significant for studying interwell transition fronts which is kept as a future research work. The constants c_0, c_1, c_2 can be obtained as (Aravind Kumar et al., 2015):

$$\begin{aligned} c_0 &= -\frac{m_t}{16L^2} 8a_0 L^2 \\ c_1 &= -\frac{m_t}{16L^2} (8a_1 L^2 + 8b_1 L) \\ c_2 &= -\frac{m_t}{16L^2} (8a_2 L^2 + 8b_2 L) \end{aligned} \tag{2}$$

where m_t is the magnetic moment of the tip mass M_t if we consider it to be made up of a magnetic material. m_t is a constant and depends on the geometric and magnetic properties of the tip mass. The geometric properties of the tip mass considered as a magnet are denoted by a_t which is its radius in the horizontal direction and $2b_t$ which is its length in the vertical direction. a_0, a_1, b_1, a_2, b_2 are coefficients of the different powers of the tip mass displacement Y_n in the Taylor series expansion of the radial (horizontal) and axial (vertical) components of the resultant magnetic field at the point where the beam is attached to the tip mass in terms of the tip mass displacement. These coefficients are computed symbolically using Mathematica and then numerically evaluated by substituting suitable values of system parameters as per our objective. Considering the tip mass to be a permanent magnet, its magnetic moment can be evaluated as (Aravind Kumar et al., 2015):

$$m_t = \frac{2B_t}{\mu_0} \pi (a_t)^2 \sqrt{(2b_t)^2 + (a_t)^2} \tag{3}$$

where B_t denotes the field strength at tip magnet's surface on its axis and μ_0 is the magnetic permeability.

Detailed derivation of the governing equations of motion for the unit-cell model for a single-mode approximation of beam displacement is provided in the Supplementary material. The single-mode reduction is intended as a leading-order description of the unit cell in the tip mass dominated regime considered here. It is expected to remain appropriate so long as the response is governed predominantly by the fundamental flexural mode, i.e., when the dynamics are controlled by the global tip motion rather than by short-wavelength bending of the beam. The approximation may lose quantitative accuracy when snap-through becomes sufficiently abrupt to generate appreciable higher-mode content, strong curvature localization develops near the clamp, or the relevant time scales approach those of the higher flexural modes. In this sense, the present formulation should be viewed as a reduced model for the collective intrawell wave dynamics and harvesting trends, rather than as a full structural representation of all beam modes. Later, while specifying the values of the system parameters, we will show that for our chosen symmetric bi-stable magnetic potential design, the distance from the unstable equilibrium point in the middle to the stable equilibrium points on either side will still be sufficiently small compared to the length of the beam for the single mode approximation to be valid. We get the final governing equations of motion from the Lagrangian of the unit cell as:

$$M_t \ddot{Y} + EI(2j-1)^4 \frac{\pi^4}{32L^3} Y + 2c_1 Y + 4c_2 Y^3 - \Theta V = 0 \tag{4}$$

$$C_p \dot{V} + \frac{V}{R_l} + \Theta \dot{Y} = 0 \tag{5}$$

where, C_p and R_l are the capacitance and load resistance of the piezoelectric circuit, V is the voltage generated and j is an integer. The piezoelectric coupling parameter Θ is given by

$$\Theta = \gamma_c (2j-1) \frac{\pi}{2L} \sin\left((2j-1) \frac{\pi L_c}{2L} \right). \tag{6}$$

where γ_c is the piezoelectric constant and L_c is the length of the piezoelectric patch. For a bimorph piezoelectric patch, γ_c can be evaluated (Friswell et al., 2012) as

$$\gamma_c = E d_{31} w_c (h + h_c) \tag{7}$$

Eq. (4) represents a duffing type oscillator equation with an electromechanical parameter coupling it to the voltage variable V in (5). The mechanical-to-electrical energy transfer can be made explicit from Eqs. (4) and (5). For the isolated unit cell, we define the mechanical energy and the electrical energy stored in the piezoelectric capacitance as

$$\mathcal{E}_m = \frac{1}{2} M_t \dot{Y}^2 + \frac{1}{2} \left[EI(2j-1)^4 \frac{\pi^4}{32L^3} + 2c_1 \right] Y^2 + c_2 Y^4, \qquad \mathcal{E}_e = \frac{1}{2} C_p V^2$$

Multiplying the mechanical equation (4) by $\dot{Y}$, the electrical equation (5) by V, and adding the two resulting expressions gives

$$\frac{d}{dt} \left(\mathcal{E}_m + \mathcal{E}_e \right) + \frac{V^2}{R_l} = 0$$

Thus, the electromechanical coupling terms do not create or destroy energy; they transfer energy from the mechanical displacement field to the electrical voltage field. The term V^2/R_l is the irreversible electrical dissipation in the load resistance and is precisely the instantaneous harvested power. For the periodic chain, the same interpretation holds after adding the conservative intercellular coupling and inertial-amplification contributions to the mechanical energy, with the total electrical dissipation obtained by summing V_n^2/R_l over the active unit cells.

We study the phase plane behavior of the tip mass $Y(t)$ where the phase space for Y is obtained by taking a two-dimensional projection on the plane $(Y, \dot{Y})$ of the actual three dimensional phase space defined by $(Y, \dot{Y}, V)$.

Mostly, we will be interested in the phase space behavior of the tip mass when it is subject to a bi-stable potential with two local minima and one local maximum. Hence, there will be three equilibrium points with two stable points corresponding to the two local minima and one unstable point corresponding to the one local maximum. For such a state to exist, a necessary criterion is that we must choose our system parameters such that $EI(2j-1)^4\frac{\pi^4}{32L^3}+2c_1<0$ and $c_2>0$. We are not saying at this point that this will be the sufficient criteria, because of the existence of the additional coupling term ΘV in (4). From existing literature (Strogatz, 1994), it is known that single degree of freedom double well oscillators when subjected to an external forcing such as a harmonic excitation can exhibit rich dynamical behavior with two stable centers corresponding to the two potential wells and one unstable saddle in the middle corresponding to the local energy maximum. Depending on the magnitude of the forcing, the oscillator can exhibit small-amplitude intrawell to large-amplitude interwell or snap-through motions leading to transient or sustained chaos. Since, we are interested in 'free' wave propagation, we do not explicitly consider any external forcing in our system. But, still because of the presence of the electromechanical coupling term, we should be interested in the phase space behavior of our unforced system while still expecting interwell oscillations arising due to large enough initial conditions leading to rich nonlinear phenomena. We take the integer $j=1$ without loss of generality.

Keeping the flexural rigidity EI untouched/preserved and simultaneously satisfying the necessary criteria for bi-stability, the distance between the base magnets $d=2d_h$, the vertical distance between the axis of the base magnets and the axis of the tip magnet d_v, the magnetic field strength at base magnets' surface on its axis B_s and the magnetic field strength at the tip magnet's surface on its axis B_t are chosen accordingly as:

$$d=2d_h=39\text{ mm},\quad d_v=32.2\text{ mm},\quad B_s=0.093\text{ T}\quad B_t=0.56\text{ T} \tag{8}$$

The coefficients c_0, c_1, c_2 are hence obtained as:

$$\begin{aligned} c_0&=-0.00133919\\ c_1&=-1.69985\\ c_2&=944.64 \end{aligned} \tag{9}$$

The constant γ_c is evaluated using Eq. (7) taking the integer j to be 1. For chosen values of system parameters shown in Table 2, γ_c is obtained as $\gamma_c=-1.03\times10^{-4}$. The magnetic permeability μ_0 has been taken as $4\pi\times10^{-7}$ in SI units.

The equilibrium points considering $V=0$ are obtained as:

$$Y_s=0,\qquad Y_s=\pm\sqrt{-\frac{\left(\frac{EI\pi^4}{32L^3}+2c_1\right)}{4c_2}} \tag{10}$$

The phase behavior is shown for two sets of initial conditions of the state space $Y(0),\dot{Y}(0),V(0)$. First, we allow only small initial perturbations of the tip mass displacement from its stable equilibrium points $\pm Y_s$ to study intrawell oscillations. Then, we study the regime of large-amplitude interwell motions by considering the initial perturbations to be significantly large for the tip mass to cross the saddle/unstable equilibrium point at $Y_s=0$ at least once. Initial velocity of tip mass and initial voltage are taken to be zero for both cases.

The phase-plane plots in Fig. 2 show that the isolated piezomagnetoelastic unit cell is not a conservative bi-stable element, but a dissipative electromechanical oscillator. For small perturbations about the stable equilibria, the trajectories in the $(Y,\dot{Y})$ projection plane spiral toward the nearest well in Fig. 2(a), while the corresponding electrical trajectories in the $(V,\dot{V})$ projection plane spiral toward the origin in Fig. 2(b). For sufficiently large initial perturbations, the tip mass undergoes transient interwell excursions across the saddle region before ultimately being captured by one of the stable wells, as seen in Fig. 2(c), and the associated voltage dynamics again collapse to the origin through larger spiral loops in Fig. 2(d). Unlike an uncoupled single degree of freedom conservative bi-stable oscillator, for which one would expect closed intrawell and interwell periodic orbits separated by two homoclinic separatrices of infinite period, the coupling terms $-\Theta V$ in Eq. (4) and $\Theta\dot{Y}$ in Eq. (5) continuously transfer mechanical energy into the electrical subsystem and dissipate it through the shunt, so that no closed or homoclinic periodic orbits persist and all projected trajectories are exponentially damped spirals. The negative value of $\gamma_c=-1.03\times10^{-4}$ calculated using (7) makes the electromechanical coupling parameter Θ to be negative, so the term $-\Theta V$ turns out to be positive. From Eq. (5), it is apparent that the voltage V will be governed by the tip mass velocity $\dot{Y}$, so essentially the term $-\Theta V$ in (4) will play a characteristic similar to positive damping or dissipation which leads to energy loss from the mechanical domain which is then captured into the electrical domain. This is precisely what makes the unit cell a meaningful building block for the periodic chain. Once such nonlinear, bi-stable, energy-converting cells are coupled spatially, one can expect wave-mediated combinations of intrawell confinement, transient snap-through, attenuation and distributed electrical extraction, thereby opening the way to both enhanced energy harvesting potential and richer collective dynamics than in a purely mechanical periodic bi-stable lattice.

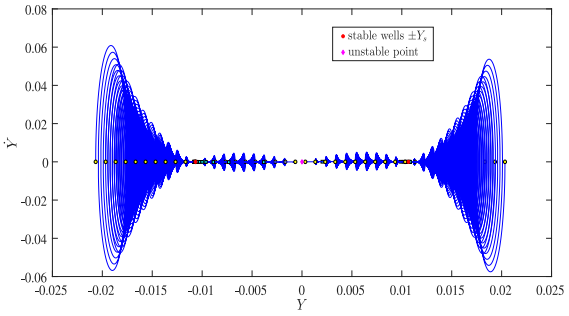

(a) Phase-plane behavior of tip mass $Y(t)$ for small perturbations from stable equilibrium position $Y_s = 10.7$ mm

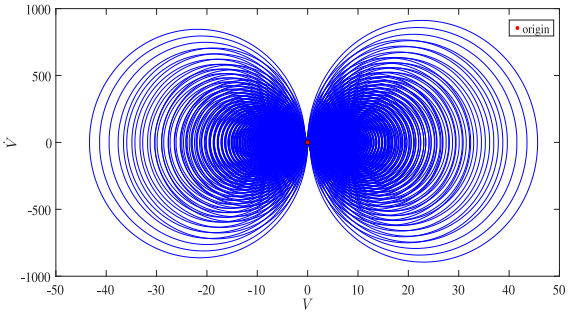

(b) Phase-plane behavior of voltage $V(t)$ for small perturbations of the tip mass from stable equilibrium position $Y_s = 10.7$ mm

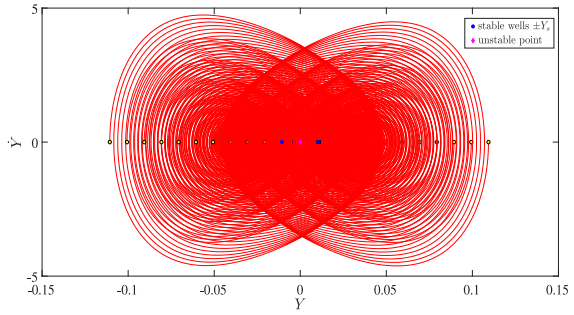

(c) Phase-plane behavior of tip mass $Y(t)$ for large enough perturbations from stable equilibrium position resulting in interwell motions

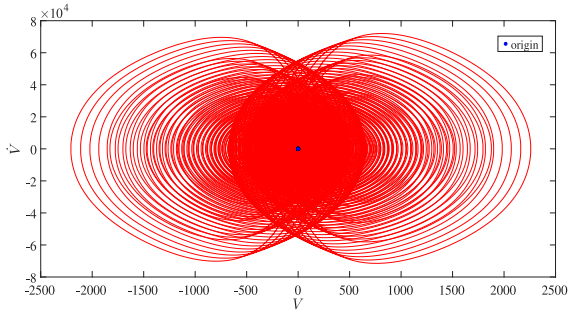

(d) [Phase-plane behavior of voltage $V(t)$ for interwell motions of the tip mass

Fig. 2. Phase-plane behavior of tip mass $Y(t)$ and voltage $V(t)$ for small intrawell oscillations of the tip mass about its stable equilibrium position and large interwell motions of the tip mass resulting in crossing the unstable saddle in the middle at least once.

3. The periodic chain

To arrive at a periodic chain composed of our repeating unit cell discussed in Section 2, we consider a one-dimensional array of N such piezomagnetoelastic beam-mass elements connected by coupling the tip mass to adjacent unit cells via horizontal linear springs and a pair of inertial amplifier masses with two rigid links as shown in Fig. 3.

The equations of motion are derived from the Lagrangian of the system and is detailed in the Supplementary material. The equations of motion governing the nth unit cell in terms of beam tip mass displacement for single- mode approximation are hence obtained as:

$$M_t\ddot{Y}_n + EI(2j-1)^4\frac{\pi^4}{32L^3}Y_n + k\left(2Y_n - Y_{n-1} - Y_{n+1}\right) + 2c_1Y_n + 4c_2Y_n^3 - \frac{m_a\cos^2\alpha}{2\sin^2\alpha}\left(2\ddot{Y}_n - \ddot{Y}_{n-1} - \ddot{Y}_{n+1}\right) - \Theta V_n = 0 \tag{11}$$

On the electrical side, considering the piezoelectric patches as a capacitor, the electrical governing differential equation remains the same as obtained for the unit cell in Section 2:

$$C_p\dot{V}_n + \frac{V_n}{R_l} + \Theta\dot{Y}_n = 0 \tag{12}$$

where R_l is the load resistor and C_p is the capacitance of the piezoelectric patches.

4. Dispersion characteristics in the linearized regime

4.1. Dispersion relation

For the linearized regime within one of the two stable wells of the total potential, we do not linearize Eq. (11) about the trivial, unstable equilibrium point $Y_n = 0$, but about a chosen stable non-zero equilibrium point Y_s. For the simplest uniform branch, the adjacent unit cells satisfy

$$Y_{n-1} = Y_n = Y_{n+1} = Y_s, \qquad \dot{Y}_n = \ddot{Y}_n = V_n = 0 \tag{13}$$

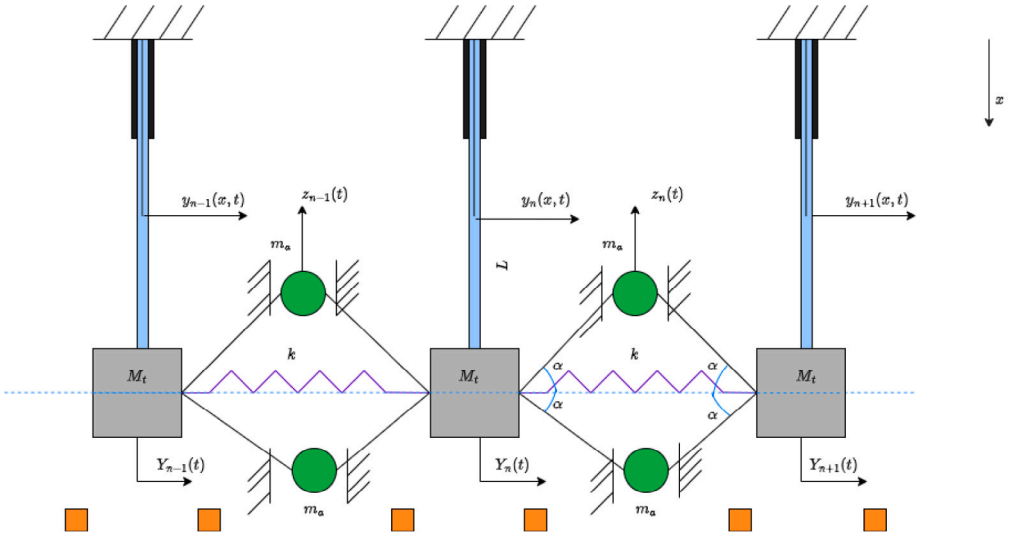

Fig. 3. The periodic piezomagnetoelastic chain.

and Eq. (11) taking the integer $j = 1$ reduces to

$$\left(k_{eff} + 2c_1\right)Y_s + 4c_2 Y_s^3 = 0 \tag{14}$$

where $k_{eff} = \frac{EI\pi^4}{32L^3}$. Hence, the equilibrium points are obtained as

$$Y_s = 0, \qquad Y_s = \pm\sqrt{-\frac{\left(k_{eff} + 2c_1\right)}{4c_2}} \tag{15}$$

The total potential corresponding to the simplest uniform branch can be written as

$$U(Y_n) = \frac{1}{2}\left(k_{eff} + 2c_1\right)Y_n^2 + c_2 Y_n^4 \tag{16}$$

For the non-zero equilibrium points to be real and stable, the local tangent stiffness at Y_s must satisfy the minimality criterion

$$K_t := \frac{\partial^2 U}{\partial Y_s^2} = k_{eff} + 2c_1 + 12c_2 Y_s^2 > 0 \tag{17}$$

Using the non-zero equilibrium points obtained in (15) gives

$$K_t = -2\left(k_{eff} + 2c_1\right) \tag{18}$$

Therefore, for a bi-stable effective net potential with two stable non-zero equilibrium points, it is required that

$$c_2 > 0, \qquad k_{eff} + 2c_1 < 0 \tag{19}$$

and in that case the trivial equilibrium point $Y_s = 0$ becomes unstable

We express the net effective displacement as $Y_s + Y_n(t)$, where $Y_n(t)$ denotes a small perturbation about the chosen stable equilibrium point Y_s. For small perturbations $|Y_n| \ll |Y_s|$, the cubic term in Eq. (11) is linearized about Y_s, so that the perturbation stiffness is modified by the additional term $12c_2 Y_s^2$. Assuming a Bloch solution for plane wave propagation in this within-well linearized regime, we can obtain the displacements of the adjacent tip masses in the $n-1$-th and $n+1$-th unit cell as:

$$\begin{aligned} Y_{n+1}(t) &= Y_n(t)e^{i\mu} \\ Y_{n-1}(t) &= Y_n(t)e^{-i\mu} \end{aligned} \tag{20}$$

where μ is the non-dimensional wavenumber

Rewriting the voltage V_n in terms of stored charge q_n gives $V_n = R_l\dot{q}_n = \frac{q_n}{C_p}$. Substituting this in the electrical equation (12) gives

$$C_p R_l \ddot{q}_n + \frac{q_n}{R_l C_p} + \Theta\dot{Y}_n = 0 \tag{21}$$

Using Bloch's solution (20) in the governing differential equation of the perturbation about the stable well, taking the integer j to be 1, gives:

$$\left(M_t - \frac{m_a \cos^2\alpha}{\sin^2\alpha}(1-\cos\mu)\right)\ddot{Y}_n + \left(2k(1-\cos\mu) + k_{eff} + 2c_1 + 12c_2 Y_s^2\right)Y_n - \Theta\frac{q_n}{C_p} = 0 \tag{22}$$

The temporal part of the solution of Eqs. (21) and (22) is sought in the form (Mosquera-Sánchez & Jr., 2021):

$$q_n(t) = Qe^{i\omega t} \tag{23}$$

where we call ω the frequency of free wave propagation in a colloquial terminology in the horizontal axial direction of the periodic chain and treat it as a book-keeping parameter as of now. By substituting (23) in (22) gives:

$$\left(M_t - \frac{m_a \cos^2\alpha}{\sin^2\alpha}(1-\cos\mu)\right)\ddot{Y}_n + \left(2k(1-\cos\mu) + k_{eff} + 2c_1 + 12c_2 Y_s^2\right)Y_n = \frac{\Theta}{C_p}Qe^{i\omega t} \tag{24}$$

Eq. (24) can be solved exactly for Y_n, which will comprise of a homogeneous solution and a particular integral and is given by

$$Y_n(t) = Y_0 e^{i\omega_0 t} + \frac{\Theta Q}{C_p m_e(\omega_0^2 - \omega^2)}e^{i\omega t} \tag{25}$$

where

$$\omega_0 = \sqrt{\frac{\left(2k(1-\cos\mu) + k_{eff} + 2c_1 + 12c_2 Y_s^2\right)}{\left(M_t - \frac{m_a\cos^2\alpha}{\sin^2\alpha}(1-\cos\mu)\right)}} \tag{26}$$

We introduce the notation

$$m_e = \left(M_t - \frac{m_a \cos^2\alpha}{\sin^2\alpha}(1-\cos\mu)\right) \tag{27}$$

Y_0 can be determined from the initial conditions imposed on the perturbation of the tip mass about the chosen stable well

Substituting (23) and (25) in (21) and equating to zero the coefficients of the exponentials, we can obtain the dispersion relation in the within-well linearized regime of the piezomagnetoelastic chain

$$\left(-\omega^2 C_p R_l Q + \frac{Q}{R_l C_p} + \frac{\Theta^2 i\omega Q}{C_p m_e(\omega_0^2 - \omega^2)}\right)e^{i\omega t} + \left(\Theta i\omega_0 Y_0\right)e^{i\omega_0 t} = 0 \tag{28}$$

Equating the coefficient of $e^{i\omega_0 t}$ to zero in (28) gives $Y_0 = 0$, which is quite expected for steady-state Bloch wave propagation within the selected stable potential well.

Equating the coefficient of $e^{i\omega t}$ to zero in (28) gives after rearranging terms the dispersion relation $\mu(\omega)$ or $\omega(\mu)$ as:

$$\cos\mu = 1 - \frac{\left(M_t\omega^2 - k_{eff} - 2c_1 - 12c_2 Y_s^2\right)\left(1 - \omega^2(R_l C_p)^2\right) + \Theta^2 i\omega R_l}{(2k + r_a\omega^2)\left(1 - \omega^2(R_l C_p)^2\right)} \tag{29}$$

where $r_a = \frac{m_a\cos^2\alpha}{\sin^2\alpha}$ is defined as the inertial amplification factor. For the linearized regime within the selected stable well, we plot the dispersion relation obtained in (29) (see Supplementary material). Real parts of the wavenumber μ correspond to propagating waves and imaginary parts correspond to attenuating waves. The parameters of the beam, piezoelectric patches, base and tip magnets are chosen as in Table 2.

The magnetic permeability μ_0 has been taken as $4\pi \times 10^{-7}$ in SI units.

We would be most likely interested in obtaining our results within a range of the magnetic potential function in terms of tip mass displacement Y_n where it preserves its bi-stable shape with two stable equilibrium positions for $Y_n(t)$ at $Y_n = \pm Y_{magnet}$ and one unstable equilibrium position in the middle at $Y_n = 0$. We also need to ensure that the conditions for existence of two stable non-zero equilibrium points of the tip mass under the net effective potential incorporating the effects from both the beam and the magnets given in (19) are satisfied. Hence, the constants c_0, c_1, c_2 and γ_c are taken as evaluated in Section 2. In the linearized regime, the dispersion profiles are shown both with and without the piezoelectric patches. Without the piezoelectric energy harvester, the linearized dispersion relation reduces to:

$$\cos\mu = 1 - \frac{\left(M_t\omega^2 - k_{eff} - 2c_1 - 12c_2 Y_s^2\right)}{(2k + r_a\omega^2)} \tag{30}$$

The angle α is taken as $\sin\alpha = 0.5$ throughout the article. For obtaining the dispersion profiles, we adopt the direct procedure, that is, fix the value of the frequency and evaluate the wavenumber by using the linearized dispersion relations (29) and (30). The detailed band structure behavior with varying structural and electrical parameters in the linearized regime is provided and discussed in the Supplementary material.

Table 2
Parameters used for the piezomagnetoelastic chain model.

Elastic Beam		Piezoelectric Patches	
Parameters	Values	Parameters	Values
ρ	2700 kg m^{-3}	L_c	30 mm
E	70 GPa	w_c	9.3 mm
w	9.5 mm	h_c	0.5 mm
h	0.25 mm	d_{31}	−210 pC N^{-1}
L	96.1 mm	C_p	51.4 nF
		R_l	20 MΩ
Base Magnets		**Tip Magnet**	
Parameters	Values	Parameters	Values
a	12.7 mm	a_t	5 mm
$2b$	6.35 mm	$2b_t$	6.35 mm
		M_t	10 g
		I_t/M_t	40.87 mm^2

It is noteworthy to mention here that the harmonic balance method (HBM) is not invoked by assuming the presence of an externally applied harmonic excitation. The present problem remains a free-wave problem. The use of HBM is justified here in a more restricted sense. After the electrical equation is rewritten in terms of the charge variable q_n, the coupled Bloch-reduced linearized Eqs. (21), (22) contain two linearly coupled fields, namely the mechanical displacement Y_n and the electrical charge q_n. When the electrical response is represented by the single-harmonic Bloch form $q_n(t) = Qe^{i\omega t}$, Eq. (22) can be written as

$$m_e(\mu)\ddot{Y}_n + K(\mu)Y_n = \frac{\Theta}{C_p}Qe^{i\omega t}, \tag{31}$$

where

$$m_e(\mu) = M_t - \frac{m_a \cos^2\alpha}{\sin^2\alpha}(1-\cos\mu) \qquad K(\mu) = 2k(1-\cos\mu) + k_{eff} + 2c_1 + 12c_2Y_s^2.$$

Thus, the mechanical equation has the same algebraic structure as a linear oscillator subjected to a harmonic driving term. However, this term is not an external force. It is generated internally by the electromechanical coupling and must be determined simultaneously from the electrical balance equation. In the linearized regime considered here, the single-harmonic balance is exact for the Bloch-wave solution, rather than an additional approximation associated with nonlinear forced-response analysis. Hence, the use of HBM for deriving the closed-form dispersion relation in (29) is justified and physically consistent.

Also, we wish to report here that we rewrote the voltage equation (12) in terms of charge q_n, i.e., Eq. (21), which resembles a second-order undamped equation, in order to explicitly apply the well-known harmonic balance method (HBM) to evaluate a closed-form expression of the dispersion relation (29) which can capture, in the most generalized regime, both the propagating and attenuating components. Had we retained the voltage equation in its original form as in (12), applying the harmonic balance method would have generated a dispersion relation that only corresponds to standing waves with $\cos\mu = 1 \implies \mu = 0$ in the irreducible Brillouin zone (IBZ).

5. Energy harvested in the linearized regime through free wave propagation

The average power harvested by the piezoelectric patch over one time period of free wave frequency ω is calculated as:

$$P_{ave} = \frac{\omega}{2\pi}\int_0^{\frac{2\pi}{\omega}} \frac{V_n^2(t)}{R_l}\,dt \tag{32}$$

To obtain $V_n(t)$ in the regime of Bloch-wave propagation, we numerically integrate Eqs. (12) and (22) in the time-domain using the fourth-order Runge–Kutta (ode45) algorithm in Matlab after rewriting $V_n = \frac{q_n}{C_p} = R_l\dot{q}_n$. We resort to convert the charge equation back to voltage while performing the time-domain integration because Eq. (21) represents a lossless second-order oscillator in q_n which when coupled to the second-order mechanical DOF (22) through Θ, the combined electromechanical system can develop an unstable pair of eigenvalues, i.e. behaving like a negative damping or active feedback and hence causing the system response to blow up in time. This will not be suitable to capture the attenuation/decay of spatial waves resulting in the harvested power through the piezoelectric patch.

To calculate the wavenumber μ for a given free wave frequency ω, we use the linearized dispersion relation derived in (29). Since the imaginary part of the wavenumber μ is accountable for mechanical energy dissipation manifesting in the harvested electrical power, we ignore the real part of μ. For complex $\mu = \alpha + i\beta$, we take $\cos\mu = \cos i\beta = \cosh\beta$. We set the value of the free wave frequency ω and evaluate α and β using (29) and run our time-domain simulation for 100 cycles of the free wave frequency and compute the power using (32) over a cycle when the initial oscillatory mechanical transients induced due to the initial displacement/velocity conditions imposed on the tip mass and hence the initial oscillatory electrical transients generated in the piezoelectric patch/harvester die out completely resulting in V_n to decay or grow respectively along a smooth envelope

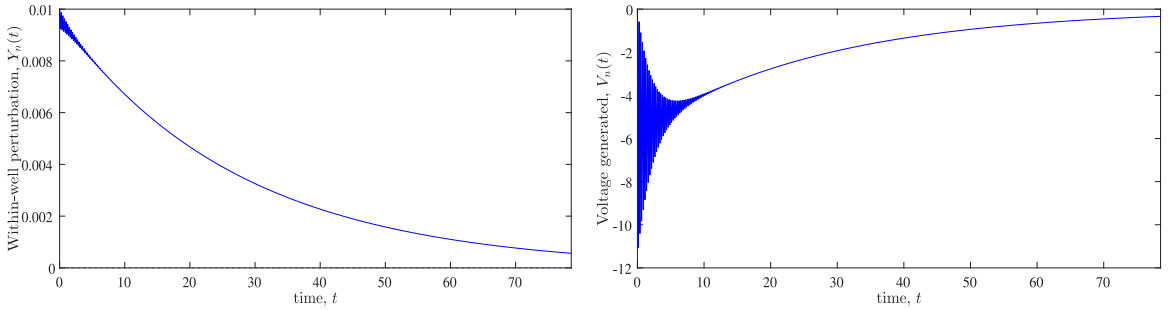

(a) Tip mass displacement $Y_n(t)$ from stable equilibrium position in the linearized regime

(b) Voltage generated $V_n(t)$ in the linearized regime

Fig. 4. Time-domain responses in the linearized regime showing the tip mass displacement $Y_n(t)$ from the stable equilibrium point at $+Y_s$ as obtained in (15) and voltage generated in the piezoelectric patch $V_n(t)$ for a representative nth unit cell, for an initial perturbation on the tip mass as $Y_n(0) = 0.01, \dot{Y}_n(0) = 0$ from the stable equilibrium position at $+Y_s$ and with values of system parameters chosen as in Table 2.

and the magnitude of the voltage, $|V_n(t)|$ becomes the largest irrespective of sign (because the power harvested depends on V_n^2) to obtain the maximum steady-state power. In an example plot shown in Fig. 4, with an input frequency value of $\omega = 8$, this seems to happen approximately at time $t = t_s \approx 20$ from an apparent visual glance at Fig. 4(b). A small initial perturbation of $Y_n(0) = Y_0 = 0.01, \dot{Y}_n(0) = 0$ has been and will be henceforth imposed on the tip mass to generate free wave motion in the periodic system in the linearized regime within the stable potential well. In a general scenario, we will use a spring stiffness value of $k = 0.1k_{eff}$, where $k_{eff} = \frac{EI\pi^4}{32L^3}$ and an inertial amplifier mass value of $m_a = 0.5M_t$ and other parameter values from Table 2. Fig. 4 is an example plot that depicts the transient voltage response of the shunted piezoelectric patch when the chain is released from an initial tip displacement with zero initial charge/voltage. As soon as the tip mass begins to move, the electromechanical coupling converts the mechanical velocity into an electrical response through the RC shunt relation (12), so V_n departs from zero once $\dot{Y}_n \neq 0$. The initial sign of the voltage is set by our sign conventions and the negative d_{31} embedded in Θ, but it does not affect the harvested energy because the electrical power scales with $\frac{V_n^2}{R_l}$. The oscillatory nature of $V_n(t)$ reflects the underlying coupled electromechanical vibration, while its decaying envelope indicates that the stored mechanical energy is progressively transferred to the electrical domain and dissipated in the resistor. After a sufficient amount of time, the decay is dominated by the electrical time constant $\tau = R_l C_p$. Using $\cos\mu = \cosh\beta$ with $\mu = \alpha + i\beta$ from (29) effectively imposes a purely evanescent (stopband) Bloch condition, modifying the effective inertia/stiffness in the mechanical equation via $1 - \cos\mu < 0$ and thereby capturing, in a single representative cell's time-domain simulation, the enhanced attenuation or energy-extraction behavior associated with the bandgap.

The physical meaning of the evanescent Bloch condition is that the displacement field contains a spatially decaying component. For a complex wavenumber $\mu = \alpha + i\beta$ with $\beta > 0$, the Bloch factor contains the attenuation term $e^{-\beta n}$, so mechanical energy injected through the initial perturbation becomes spatially localized instead of propagating indefinitely through the chain. This localization increases the effective residence of vibrational energy near the active piezoelectric cells, allowing the electromechanical coupling to convert a larger fraction of the localized mechanical energy into voltage before it is dissipated through the load resistance. Hence, the evanescent component should not be interpreted only as wave suppression; in the present electromechanical chain, it provides the physical pathway by which stop-band localization is translated into enhanced electrical dissipation and harvested power.

6. Dependence of maximum steady-state power on free wave frequency

By free-wave frequency, we refer to the characteristic frequency associated with free wave propagation generated solely by initial conditions in the absence of any sustained external forcing or base excitation. Therefore, ω should not be interpreted as an independently prescribed excitation frequency. Instead, it is used as a dispersion-based book-keeping parameter that parameterizes the admissible free-wave components supported by the chosen structural, magnetic, inertial, and electrical properties of the chain. In practice, sweeping ω is equivalent to scanning the corresponding family of system designs through the dispersion relation, since the associated wavenumber, effective inertia, effective stiffness, and harvested power are all determined by the coupled system parameters. Once a maximum-power condition is imposed later in Section 7.1.2, the optimum value $\omega = \omega_e$ is no longer arbitrary, but emerges from the design parameters and the imposed initial state. In the nonlinear regime, this interpretation is further amplitude-dependent, because the initial perturbation fixes the intrawell oscillation amplitude and thereby modifies the nonlinear dispersion branch on which the corresponding free-wave frequency is evaluated.

The free wave frequency ω (which we consider as a book-keeping parameter, again re-emphasizing the fact that it has to be and will be prescribed essentially by accordingly choosing the values of the system design parameters) is swept over a range of values and the power harvested over a cycle when initial oscillatory transients generated due to the initial conditions imposed on the tip mass die out completely and voltage generated is maximum in magnitude, is evaluated and plotted with ω. We use a value of spring stiffness coefficient of $k = 0.1k_{eff}$, inertial amplifier mass of $m_a = 0.5M_t$ and keep the values of the other parameters fixed as defined in Table 2. We also impose two more conditions for practical feasibility:

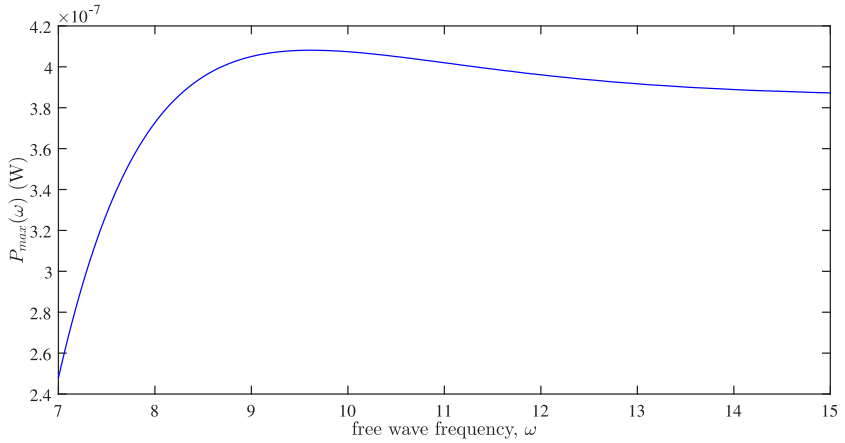

Fig. 5. Power harvested in the linearized regime over the cycle of maximum steady-state voltage amplitude plotted with free wave frequency ω for an initial perturbation on the tip mass as $Y_n(0) = 0.01, \dot{Y}_n(0) = 0$ from the stable equilibrium position.

- $m_e(\mu) = \left(M_t - \frac{m_a \cos^2 \alpha}{\sin^2 \alpha}(1 - \cos \mu) \right) \neq 0$
- $K(\mu) = \left(2k(1 - \cos \mu) + k_{eff} + 2c_1 + 12c_2 Y_s^2 \right) > 0$ from Eq. (22).

Fig. 5 shows the power harvested in the linearized regime over the cycle of maximum steady-state voltage amplitude from free wave motion through our chosen piezomagnetoelastic periodic chain for a range of free wave frequencies ω with initial conditions for the tip mass chosen the same as in Fig. 4. It is observed that the maximum steady-state power or in other words, the maximum steady-state energy is harvested in the linearized regime through the piezoelectric patch from free wave motion through our system at a particular value of frequency ω (which happens to be approximately around $\omega \approx 9.5$ in Fig. 5), while keeping the structural and electrical parameters of the system fixed. We denote this frequency corresponding to maximum harvested energy/power in the steady state as $\omega = \omega_e \approx 9.5$ for our chosen system parameters.

To generate the curve depicting the dependence of maximum steady-state power on non-dimensional frequency ω, we have extracted the voltage over one time period/cycle of our colloquially used free wave frequency ω after a certain settling time when the initial oscillatory transients die out and the voltage $\tilde{V}_n(\tau)$ evolves along a smooth envelope. Later, we will show in 7.1.2 that there is instead a more systematic and consistent method to choose the time period of this cycle based on the system eigenvalues in the intrawell linearized regime.

As of now, we have used a value of the settling time as $t_s = 20$ from our visual approximation from Fig. 4(b) which was obtained by setting $\omega = 8$ which lies within the range of ω swept in Fig. 5. We have used this same value of visually approximated settling time to obtain the power vs frequency curve shown in Fig. 5, for every input frequency ω over the sweeping interval chosen. Later, we will propose a systematic analytical approach in Section 7.3 to derive a compact closed-form expression for this settling time which we will denote by $t_s(\omega)$ in terms of the input free wave frequency ω or in other words the system parameters. We will also show that the optimum frequency value $\omega = \omega_e$ corresponding to the peak power and the magnitude of the peak power harvested in the steady-state regime denoted by the isolated peak in Fig. 5 are both dependent on this settling time $t_s(\omega)$.

In the Supplementary material, the varying behavior of this maximum steady-state power with the structural and electrical parameters is provided.

7. An analytical approach to characterize harvested power in the linear regime

7.1. Analytical framework in the time-domain to find optimum frequency for maximum steady-state power

7.1.1. Modal expansion of state space vector

In the linear regime, we can convert Eqs. (12) and (22) to an equivalent state space form $\mathbf{A}\dot{\mathbf{y}} + \mathbf{B}\mathbf{y} = \mathbf{0}$ by choosing an appropriate state vector $\mathbf{y} = \begin{Bmatrix} Y_n(t) \\ \dot{Y}_n(t) \\ V_n(t) \end{Bmatrix}$. The matrices $\mathbf{A}$ and $\mathbf{B}$ are obtained as:

$$\mathbf{A}=\begin{bmatrix}1 & 0 & 0\\ 0 & m_e(\mu) & 0\\ 0 & 0 & C_p\end{bmatrix},\mathbf{B}=\begin{bmatrix}0 & -1 & 0\\ K(\mu) & 0 & -\Theta\\ 0 & \Theta & \frac{1}{R_l}\end{bmatrix} \tag{33}$$

where $m_e(\mu)$ and $K(\mu)$ have already been defined in Section 6.

We use the same logic as in Section 6, that we use the imaginary part of wavenumber μ from (29) which is responsible for wave attenuation/energy dissipation responsible in energy being harvested by the piezoelectric patch. So, we take $\cos\mu=\cos(\alpha+i\beta)\approx\cosh\beta$. Since we take $\cos\mu$ to be real, our $m_e(\mu)$ and $K(\mu)$ will also be real and so will be matrices $\mathbf{A}$ and $\mathbf{B}$.

The state space equation with matrices defined in (33) can be converted into an eigenvalue problem $\dot{\mathbf{y}}=\mathbf{S}\mathbf{y}$ where $\mathbf{S}=-\mathbf{A}^{-1}\mathbf{B}$. Assuming a solution of the form $\mathbf{y}=\mathbf{y}_0e^{\lambda t}$, gives the standard eigenvalue problem $\mathbf{S}\mathbf{y}_0=\lambda\mathbf{y}_0$. Setting the determinant $|\mathbf{S}-\lambda I|=0$ for non-trivial solutions of $\mathbf{y}_0$, we get the characteristic polynomial in terms of λ as:

$$\lambda^3+a\lambda^2+b\lambda+c=0 \tag{34}$$

where $a=\frac{1}{R_lC_p},b=\frac{K(\mu)}{m_e(\mu)}+\frac{\Theta^2}{m_e(\mu)C_p},c=\frac{K(\mu)}{m_eR_lC_p}$. For convenience, we denote these coefficients by physically meaninngful lumped quantities as:

$$\tau=R_lC_p,\omega_m^2=\frac{K(\mu)}{m_e(\mu)},\kappa=\frac{\Theta^2}{m_e(\mu)C_p} \tag{35}$$

By applying Cardano's formula for cubic equations, solving (34) gives the roots λ as:

$$\lambda_l=2\sqrt{-\frac{p}{3}}\cos\left(\frac{1}{3}\arccos\left(\frac{3q}{2p}\sqrt{-\frac{3}{p}}\right)-\frac{2\pi l}{3}\right)-\frac{1}{3\tau},\qquad l=1,2,3 \tag{36}$$

where $p=(\omega_m^2+\kappa)-\frac{1}{3\tau^2},\quad q=\frac{2}{27\tau^3}+\frac{2\omega_m^2-\kappa}{3\tau}$. For all three real roots of λ, we should choose our system parameters such that $p<0$. Once we find the eigenvalues λ_l, we can find the eigenvectors $v_l,\quad l=0,1,2$ by substituting λ_l in the eigenvalue problem. In the linear regime, using modal superposition, the state vector $\mathbf{y}(t)$ can always be written as:

$$\mathbf{y}(t)=\begin{Bmatrix}Y_n(t)\\ \dot{Y}_n(t)\\ V_n(t)\end{Bmatrix}=c_1v_1e^{\lambda_1t}+c_2v_2e^{\lambda_2t}+c_3v_3e^{\lambda_3t} \tag{37}$$

where $c_1,\ c_2,\ c_3$ are constants which can be determined from the initial conditions or initial state $\mathbf{y}(0)=\mathbf{y}_0$ by inverting the eigenvector matrix $\mathbf{V}=[v_1\ \ v_2\ \ v_3]$, whose columns are the eigenvectors $v_l,\quad l=1,2,3$. If the eigenvalues of $\mathbf{S}$ are distinct, which is the most generalized case, then the eigenvectors v_l will always be linearly independent which means that the eigenvector matrix constructed by using those eigenvectors as its columns will always be non-singular and hence invertible. So, in the most generalized case, we can always find out the constant coefficients $c_1,\ c_2,\ c_3$ by choosing our desired non-zero initial conditions or initial state of the system.

The eigenvalues and hence the eigenvectors will be dependent on the system parameters and the wavenumber μ related to free wave propagation through our system in the linearized regime. Here, we have posed a general eigenvalue problem for free response of linear systems whereas in the next section Section 7.1.2, we will show how the book-keeping parameter ω comes into the picture through the stiffness term $K\left(\mu(\omega)\right)$ or equivalently $B(\omega)$ in the regime of free wave propagation through linear periodic systems.

7.1.2. Step-by-step analytical formulation for obtaining maximum steady-state power

Using the Bloch reduction and writing $V_n=q_n/C_p$, the linearized governing equations can be written as

$$m_e(\mu)\,\ddot{Y}_n(t)+K(\mu)\,Y_n(t)-\Theta\,V_n(t)=0 \tag{38}$$

$$C_p\,\dot{V}_n(t)+\frac{1}{R_l}V_n(t)+\Theta\,\dot{Y}_n(t)=0 \tag{39}$$

where

$$m_e(\mu)=M_t-r_a\left(1-\cos\mu\right) \tag{40}$$

$$K(\mu)=2k\left(1-\cos\mu\right)+k_{eff}+2c_1+12c_2Y_s^2 \tag{41}$$

For each prescribed free-wave frequency ω, compute $\mu(\omega)$ from the linearized dispersion relation (29), and then treat $\cos\mu$ (hence m_e and K) as frequency-dependent through $\mu(\omega)$:

$$\cos\mu(\omega)=1-\frac{\left(M_t\omega^2-k_{eff}-2c_1-12c_2Y_s^2\right)\left(1-\omega^2(R_lC_p)^2\right)+\Theta^2\,i\omega R_l}{\left(2k+r_a\omega^2\right)\left(1-\omega^2(R_lC_p)^2\right)} \tag{42}$$

For 'purely-evanescent' approximation used in Section 5, rewrite $\cos\mu$ as $\cosh\beta$ with $\beta=|Im(\mu)|$. Hence, define β in closed-form as $\beta=sgn*\left|Im\left\{\arccos\left(\chi(\omega)\right)\right\}\right|=sgn*\left|Im\left(\arccos\left[1-\frac{\left(M_t\omega^2-\frac{EI\pi^4}{32L^3}-2c_1-12c_2Y_s^2\right)\left(1-\omega^2(R_lC_p)^2\right)+\Theta^2i\omega R_l}{(2k+r_a\omega^2)\left(1-\omega^2(R_lC_p)^2\right)}\right]\right)\right|$ from (29), with the sgn

function defined as $sgn = \mathrm{sgn}\left[Re\left(1 - \frac{\left(M_t\omega^2 - \frac{EI\pi^4}{32L^3} - 2c_1 - 12c_2Y_s^2\right)\left(1-\omega^2(R_lC_p)^2\right)+\Theta^2 i\omega R_l}{(2k+r_a\omega^2)\left(1-\omega^2(R_lC_p)^2\right)}\right)\right]$, if the argument inside square brackets is $\neq 0$, or $sgn = 1$ when the argument inside square brackets is 0.

Choose the state vector

$$\mathbf{y}(t) = \begin{bmatrix} y_1(t) \\ y_2(t) \\ y_3(t) \end{bmatrix} = \begin{bmatrix} Y_n(t) \\ \dot{Y}_n(t) \\ V_n(t) \end{bmatrix} \tag{43}$$

Then (38)–(39) are equivalent to

$$A(\omega)\,\dot{\mathbf{y}}(t) + B(\omega)\,\mathbf{y}(t) = \mathbf{0} \tag{44}$$

with

$$A(\omega) = \begin{bmatrix} 1 & 0 & 0 \\ 0 & m_e(\omega) & 0 \\ 0 & 0 & C_p \end{bmatrix}, \qquad B(\omega) = \begin{bmatrix} 0 & -1 & 0 \\ K(\omega) & 0 & -\Theta \\ 0 & \Theta & 1/R_l \end{bmatrix} \tag{45}$$

If $m_e(\omega) \neq 0$ and $C_p > 0$, define the standard state matrix

$$\dot{\mathbf{y}}(t) = S(\omega)\,\mathbf{y}(t), \qquad S(\omega) = -A(\omega)^{-1}B(\omega) = \begin{bmatrix} 0 & 1 & 0 \\ -\frac{K(\omega)}{m_e(\omega)} & 0 & \frac{\Theta}{m_e(\omega)} \\ 0 & -\frac{\Theta}{C_p} & -\frac{1}{R_lC_p} \end{bmatrix} \tag{46}$$

Let $(\lambda_i, \mathbf{v}_i, \mathbf{w}_i)$, $i = 1, 2, 3$, be the right/left eigen-triples of $S(\omega)$:

$$S(\omega)\mathbf{v}_i(\omega) = \lambda_i(\omega)\mathbf{v}_i(\omega), \qquad \mathbf{w}_i(\omega)^{\mathsf{T}}S(\omega) = \lambda_i(\omega)\mathbf{w}_i(\omega)^{\mathsf{T}}, \qquad \mathbf{w}_i^{\mathsf{T}}\mathbf{v}_j = \delta_{ij} \tag{47}$$

Then for initial condition $\mathbf{y}(0) = \mathbf{y}_0$,

$$\mathbf{y}(t) = \sum_{i=1}^{3}\left(\mathbf{w}_i^{\mathsf{T}}\mathbf{y}_0\right)\mathbf{v}_i\, e^{\lambda_i t} \tag{48}$$

The voltage is the third component:

$$V_n(t) = \mathbf{e}_3^{\mathsf{T}}\mathbf{y}(t) = \sum_{i=1}^{3} c_i(\omega)\, e^{\lambda_i(\omega)t}, \qquad c_i(\omega) = \left(\mathbf{e}_3^{\mathsf{T}}\mathbf{v}_i(\omega)\right)\left(\mathbf{w}_i(\omega)^{\mathsf{T}}\mathbf{y}_0\right) \tag{49}$$

where $\mathbf{e}_3 = [0\ 0\ 1]^{\mathsf{T}}$.

Over a single wave period $T(\omega) = 2\pi/\omega$, starting at time t_s,

$$P_{ave}(t_s, \omega) = \frac{1}{R_l\,T(\omega)}\int_{t_s}^{t_s+T(\omega)} V_n(t)^2\, dt \tag{50}$$

Substituting (49) gives the closed-form double-sum:

$$P_{ave}(t_s, \omega) = \frac{1}{R_l\,T}\sum_{i=1}^{3}\sum_{j=1}^{3}\frac{c_ic_j\, e^{(\lambda_i+\lambda_j)t_s}\left(e^{(\lambda_i+\lambda_j)T} - 1\right)}{\lambda_i + \lambda_j}, \qquad T = \frac{2\pi}{\omega} \tag{51}$$

Optimality condition for peak-power frequency. Define $t_0(\omega)$ as an interior maximizer of $P_{ave}(t_s, \omega)$ in the post-transient regime. A necessary condition for obtaining the maximum steady-state power is

$$E(t_0, \omega) := \frac{\partial P_{ave}}{\partial t_0}(t_s, \omega) = 0 \tag{52}$$

The peak-power frequency ω_e (peak of $\bar{P}$ after optimizing over t_0) satisfies

$$F(t_0(\omega), \omega) := \frac{\partial P_{ave}}{\partial \omega}\left(t_0(\omega), \omega\right) = 0 \tag{53}$$

Let, $T = \frac{2\pi}{\omega}$, $\quad B_{ij}(\omega) = \lambda_i(\omega) + \lambda_j(\omega)$, $\quad B'_{ij}(\omega) = \lambda'_i(\omega) + \lambda'_j(\omega)$ and denote $c'_i = dc_i/d\omega$, $\lambda'_i = d\lambda_i/d\omega$. Then the condition $F = 0$ can be written as

$$0 = F(t_0, \omega) = \underbrace{e^{B_{11}t_0}\,\mathcal{G}_{11}}_{(1,1)} + 2\underbrace{e^{B_{12}t_0}\,\mathcal{G}_{12}}_{(1,2)} + 2\underbrace{e^{B_{13}t_0}\,\mathcal{G}_{13}}_{(1,3)} + \underbrace{e^{B_{22}t_0}\,\mathcal{G}_{22}}_{(2,2)} + 2\underbrace{e^{B_{23}t_0}\,\mathcal{G}_{23}}_{(2,3)} + \underbrace{e^{B_{33}t_0}\,\mathcal{G}_{33}}_{(3,3)} \tag{54}$$

where, for each pair (i, j),

$$\mathcal{G}_{ij} = \left(c'_ic_j + c_ic'_j\right)\frac{e^{B_{ij}T} - 1}{B_{ij}} + c_ic_j\,t_0\,B'_{ij}\,\frac{e^{B_{ij}T} - 1}{B_{ij}} + c_ic_j\left(\frac{e^{B_{ij}T}(B_{ij}T - 1) + 1}{B_{ij}^2}\right)B'_{ij}$$

$$+ \frac{1}{\omega} c_i c_j \frac{e^{B_{ij}T} - 1}{B_{ij}} - \frac{T}{\omega} c_i c_j e^{B_{ij}T} \tag{55}$$

Substitute $B_{ij} = \lambda_i + \lambda_j$ explicitly. For instance, $B_{12} = \lambda_1 + \lambda_2$, $\implies \frac{e^{B_{12}T}-1}{B_{12}} = \frac{e^{(\lambda_1+\lambda_2)T}-1}{\lambda_1+\lambda_2}$

Applying this substitution to all $\mathcal{G}_{ij}$ in (54) gives an explicit transcendental equation in terms of $\{\lambda_i(\omega), \lambda_i'(\omega), c_i(\omega), c_i'(\omega)\}$, the location t_0 for maximum steady-state power, and $T = 2\pi/\omega$. Solving this transcendental equation gives the value for ω and hence $t_0(\omega)$ in terms of known or designed system parameters, so that they do not remain arbitrary external inputs or book-keeping parameters henceforth and provide a design/operating range of our system parameters to obtain maximum harvested power through free wave motion in a steady state. The only thing remaining is to establish the same for the settling time $t_s(\omega)$ in terms of system parameters which we will derive in Section 7.3.

As stated, the final optimality condition obtained from (49)–(54) is transcendental in nature. This is expected because the harvested-power expression contains modal coefficients, eigenvalues, and exponential terms, all of which depend implicitly on the free-wave frequency through the coupled electromechanical dispersion relation. Therefore, the resulting condition should not be interpreted as an elementary closed-form formula for the optimum frequency. Rather, it provides a mathematically tractable residual whose roots correspond to stationary values of the averaged harvested power. The physical interpretation of this result is that the optimum harvested power is governed by the combined influence of the electromechanical eigenstructure, the decay of the modal response, and the selected post-transient averaging interval. The eigenvalues determine the decay rate and oscillatory content of the response, whereas the modal coefficients determine how strongly each mode contributes to the voltage generated across the load resistance. Consequently, the transcendental form of the optimality condition arises naturally from retaining the complete state-space and eigenvalue dependence of the coupled system. Although this makes the analytical expression relatively dense, it also preserves the full parameter dependence required for a systematic optimization of the harvested energy.

Such transcendental equations can be solved using standard numerical root-finding or optimization techniques, including the Newton–Raphson method, secant method, bisection method, Brent's method, fixed-point iteration, continuation methods, or derivative-free optimization algorithms. In the present study, the final optimality condition is evaluated numerically in Matlab, and the corresponding optimum frequency and maximum averaged harvested power are obtained from the numerical solution of the derived transcendental equation.

In the intrawell linearized regime, for each fixed free-wave parameter ω, the reduced electromechanical model remains a Linear Time Invariant (LTI) system and the actual oscillatory content of the post-transient response is governed by the dominant complex-conjugate poles of the state matrix $S(\omega)$, which we write as $s_{2,3}(\omega) = -\sigma_{\text{osc}}(\omega) \pm i\omega_d(\omega)$. Therefore, although ω enters the Bloch reduction through the effective coefficients $m_e(\omega)$ and $K(\omega)$, the cycle over which the steady-state harvested power is evaluated should be chosen from the damped modal period $T_d(\omega) = 2\pi/\omega_d(\omega)$ rather than from the book-keeping period $2\pi/\omega$. Accordingly, after estimating the transient-settling time either from a visual approximation or later from a systematic derivation (as shown in 7.3), we evaluate the post-transient power by sliding a window of length $T_d(\omega)$ over the response and defining

$$P_{ave}(t_0, \omega) = \frac{1}{R_l T_d(\omega)} \int_{t_0}^{t_0+T_d(\omega)} V_n^2(t)\, dt \tag{56}$$

with the maximum steady-state power obtained as

$$P_{max}(\omega) = \max_{t_0 \geq t_s(\omega)} P_{ave}(t_0, \omega) \tag{57}$$

This refinement makes the time-domain power metric consistent with the actual oscillatory transient observed in $V_n(t)$ and removes the inconsistency that arises when the averaging window is prescribed from ω while the post-transient cycle is in fact controlled by $\omega_d(\omega)$

7.2. An alternative analytical approach in the Laplace domain to find maximum steady-state power and the corresponding optimum frequency and the extent of its validity

7.2.1. Transfer function/frequency response evaluation

Let the Laplace transforms of displacement and voltage be denoted by

$$\mathcal{L}\{Y_n(t)\} = Y_n(s) \qquad \mathcal{L}\{V_n(t)\} = V_n(s) \tag{58}$$

Using standard identities

$$\mathcal{L}\{\dot{Y}_n\} = sY_n(s) - Y_n(0) \tag{59}$$

$$\mathcal{L}\{\ddot{Y}_n\} = s^2 Y_n(s) - sY_n(0) - \dot{Y}_n(0) \tag{60}$$

$$\mathcal{L}\{\dot{V}_n\} = sV_n(s) - V_n(0) \tag{61}$$

Applying $\mathcal{L}\{\cdot\}$ to (38)–(39) gives the algebraic system

$$\left(m_e s^2 + K\right) Y_n(s) - \Theta V_n(s) = m_e \left(sY_n(0) + \dot{Y}_n(0)\right) \tag{62}$$

$$\Theta s\, Y_n(s) + \left(C_p s + \frac{1}{R_l}\right) V_n(s) = C_p V_n(0) + \Theta Y_n(0) \tag{63}$$

Equivalently in matrix form we obtain

$$\underbrace{\begin{bmatrix} m_e s^2 + K & -\Theta \\ \Theta s & C_p s + \dfrac{1}{R_l} \end{bmatrix}}_{\mathbf{D}(s;\mu)} \begin{bmatrix} Y_n(s) \\ V_n(s) \end{bmatrix} = \begin{bmatrix} m_e \left(s Y_n(0) + \dot{Y}_n(0) \right) \\ C_p V_n(0) + \Theta Y_n(0) \end{bmatrix} \tag{64}$$

By Cramer's rule, we define the common denominator, $\Delta(s;\mu) = \left(m_e s^2 + K\right)\left(C_p s + \frac{1}{R_l}\right) + \Theta^2 s$. Then the voltage in the Laplace domain is obtained as:

$$V_n(s) = \frac{\left(m_e s^2 + K\right)\left(C_p V_n(0) + \Theta Y_n(0)\right) - \Theta s\, m_e \left(s Y_n(0) + \dot{Y}_n(0)\right)}{\Delta(s;\mu)} \tag{65}$$

For the free response initial conditions used throughout: $Y_n(0) = Y_0, \dot{Y}_n(0) = 0, V_n(0) = 0$, the expression in (65) simplifies exactly to

$$V_n(s) = \frac{\Theta\, K(\mu)\, Y_0}{\Delta(s;\mu)} \tag{66}$$

Defining the complex frequency-axis voltage $\hat{V}_n(\omega) \equiv V_n(i\omega)$, we get

$$\hat{V}_n(\omega) = \frac{\Theta K(\omega)\, Y_0}{\left(i\omega C_p + \frac{1}{R_l}\right)\left(K(\omega) - m_e(\omega)\omega^2\right) + i\omega\Theta^2} \tag{67}$$

Using the one-period average power definition, the harmonic-amplitude form is

$$P(\omega) = \frac{1}{2R_l}\left|\hat{V}_n(\omega)\right|^2 \tag{68}$$

Substituting the expression for $\hat{V}_n(\omega)$ gives

$$P(\omega) = \frac{1}{2R_l}\left|\frac{\Theta K(\omega)\, Y_0}{\left(i\omega C_p + \frac{1}{R_l}\right)\left(K(\omega) - m_e(\omega)\omega^2\right) + i\omega\Theta^2}\right|^2 \tag{69}$$

Let $N(\omega) \equiv \Theta K(\omega)\, Y_0$, $D(\omega) \equiv \left(i\omega C_p + \frac{1}{R_l}\right)\left(K(\omega) - m_e(\omega)\omega^2\right) + i\omega\Theta^2$. Then the expression for power is obtained as

$$P(\omega) = \frac{1}{2R_l}\left|\frac{N(\omega)}{D(\omega)}\right|^2 \tag{70}$$

The condition for obtaining maximum power is set in the conventional form as:

$$\frac{dP(\omega)}{d\omega} = 0 \quad \Longleftrightarrow \quad Re\left\{\frac{N'(\omega)}{N(\omega)} - \frac{D'(\omega)}{D(\omega)}\right\} = 0 \tag{71}$$

Since $N'(\omega)/N(\omega) = K'(\omega)/K(\omega)$, we only need $D'(\omega)$, Introducing

$$Q(\omega) \equiv K(\omega) - m_e(\omega)\omega^2 \tag{72}$$

We get

$$D(\omega) = \left(i\omega C_p + \frac{1}{R_l}\right)Q(\omega) + i\omega\Theta^2 \tag{73}$$

$$D'(\omega) = iC_p\, Q(\omega) + \left(i\omega C_p + \frac{1}{R_l}\right)Q'(\omega) + i\Theta^2 \tag{74}$$

where $Q'(\omega) = K'(\omega) - m_e'(\omega)\omega^2 - 2m_e(\omega)\omega$. Finally, $K'(\omega)$ and $m_e'(\omega)$ follow from introducing the notation $\chi(\omega) = \cos\mu(\omega)$ and using the frequency-dependent relations (40) and (41) as :

$$\begin{aligned} K'(\omega) &= -2k\,\chi'(\omega) \\ m_e'(\omega) &= r_a\,\chi'(\omega) \end{aligned} \tag{75}$$

Now from dispersion relation (42), it can be seen that $\chi(\omega) = \cos\mu(\omega)$ is a complex number with non-zero real and imaginary parts in the most generalized case. Since while working in the Laplace domain, we cannot have complex coefficients of variables, we use our previous logic that we are interested only in the imaginary component of the wavenumber μ which is responsible for wave attenuation and hence manifestation of the harvested energy. Hence, we take $\cos\mu(\omega) = \cosh\beta(\omega)$, as done in Section 7.1.2.

Therefore, the frequency-dependent effective mass and stiffness can be written as

$$m_e(\omega) = M_t - r_a\left(1 - \cosh\beta(\omega)\right) \qquad K(\omega) = 2k\left(1 - \cosh\beta(\omega)\right) + k_{eff} + 2c_1 \tag{76}$$

Their derivatives follow by the chain rule

$$\frac{d}{d\omega}\cosh\beta(\omega) = \sinh\beta(\omega)\,\beta'(\omega) \tag{77}$$

so that we obtain

$$K'(\omega) = -2k\ \sinh\beta(\omega)\,\beta'(\omega) \qquad m_e'(\omega) = r_a\ \sinh\beta(\omega)\,\beta'(\omega) \tag{78}$$

Hence,

$$Q'(\omega) = -\left(2k + r_a\omega^2\right)\sinh\beta(\omega)\,\beta'(\omega) - 2m_e(\omega)\omega \tag{79}$$

Substituting the above expressions into the stationary condition (71) gives the scalar equation for the optimum free-wave frequency $\omega = \omega_e$ as:

$$Re\left\{\frac{-2k\ \sinh\beta(\omega)\,\beta'(\omega)}{K(\omega)} - \frac{iC_p\,Q(\omega) + \left(i\omega C_p + \frac{1}{R_l}\right)Q'(\omega) + i\Theta^2}{\left(i\omega C_p + \frac{1}{R_l}\right)Q(\omega) + i\omega\Theta^2}\right\} = 0 \tag{80}$$

where

$$Q(\omega) = K(\omega) - m_e(\omega)\omega^2 \tag{81}$$

and

$$K(\omega) = 2k\,(1 - \cosh\beta(\omega)) + k_{eff} + 2c_1 \qquad m_e(\omega) = M_t - r_a\,(1 - \cosh\beta(\omega)) \tag{82}$$

together with the feasibility constraints

$$\omega > 0, \qquad m_e(\omega) \neq 0, \qquad K(\omega) > 0 \tag{83}$$

And in practice as mentioned before, $\beta(\omega)$ is evaluated from

$$\beta(\omega) = \left|Im\left\{\arccos\left(\chi(\omega)\right)\right\}\right| \tag{84}$$

where $\chi(\omega) = 1 - \frac{\left(M_t\omega^2 - k_{eff} - 2c_1 - 12c_2Y_s^2\right)\left(1-\omega^2(R_lC_p)^2\right) + \Theta^2 i\omega R_l}{(2k + r_a\omega^2)\left(1-\omega^2(R_lC_p)^2\right)}$. $\beta'(\omega)$ can be obtained numerically (finite differences) or by analytic differentiation of $\mu(\omega) = \arccos(\chi(\omega))$

$$\mu'(\omega) = -\frac{\chi'(\omega)}{\sqrt{1-\chi(\omega)^2}} \qquad \beta'(\omega) = \mathrm{sgn}(Im\{\mu(\omega)\})\,Im\{\mu'(\omega)\} \tag{85}$$

7.2.2. Extent of validity of the Laplacian framework and possible advantages

Remark on Laplace-domain versus time-domain optima. In the Laplace-domain framework, we evaluate the voltage in the complex-frequency domain as $V_n(s)$ and obtain a frequency-response magnitude by restricting to the imaginary axis, $s = i\omega$, which leads to a closed-form power estimate $P(\omega) = \frac{|V_n(i\omega)|^2}{2R_l}$.

This is useful because it enables an analytical prediction of the attainable (peak) power level without explicit time stepping and it reveals how the electrical and mechanical parameters enter the power expression. However, maximizing $|V_n(i\omega)|$ is a purely frequency-domain criterion that does not enforce the same time-domain constraint used in our definition of P_{max} in Sections 5 and 7.1.2, where the power is computed over the one-period window that achieves the largest post-transient average after a prescribed steady-time threshold $t \geq t_0$ when the displacement and consequently voltage evolve along a smooth envelope. In the present free-response setting, $V_n(t)$ is a superposition of damped modal contributions, so the cycle that yields the largest voltage magnitude after transients depends not only on frequency content but also on modal decay rates and on the chosen steady-time window. Consequently, the Laplace-domain maximizer obtained directly from $|V_n(i\omega)|$ can reproduce the correct peak power magnitude while predicting an 'optimal' ω that is shifted relative to the time-domain optimum defined with the post-transient windowing rule. To obtain an optimal frequency that is consistent with the deterministic time-domain metric, the Laplace-domain solution must be mapped back to $V_n(t)$ via an inverse Laplace transform or an equivalent modal reconstruction, after which the same t_0 based windowing constraint can be enforced during the optimization.

Fig. 6 shows this disadvantage of the Laplacian approach in predicting the true optimum frequency requirement of the system to generate maximum steady-state power. However, the Laplacian framework provides an excellent approach to obtain an approximate close-form expression for the settling time $t_s(\omega)$ in terms of the system parameters without having to actually evaluate the roots of the cubic characteristic polynomial (34) of the coupled electromechanical system, which we will show in the next Section 7.3, where we will use the concept of settling time in a sort of inverse Laplacian framework to enforce the time constraint mentioned previously in Section 6 and Section 7.1.2.

7.3. An approximate analytical approach to characterize the settling time t_s mentioned in Section 7.1.2

As we have mentioned before in Sections 5 and 7.1.2, we intend to extract the voltage at a time when the initial oscillatory transients die out and the magnitude of the voltage generated in the harvester $|V_n(t)|$ is maximum. Finding an exact closed-form solution for this settling time $t_s(\omega)$ might be challenging. So, we use an approximate approach to evaluate the expression for this time instant. We use the example time-domain response of the tip mass $Y_n(t)$ shown in Fig. 4(a), which seems to be a superposition of

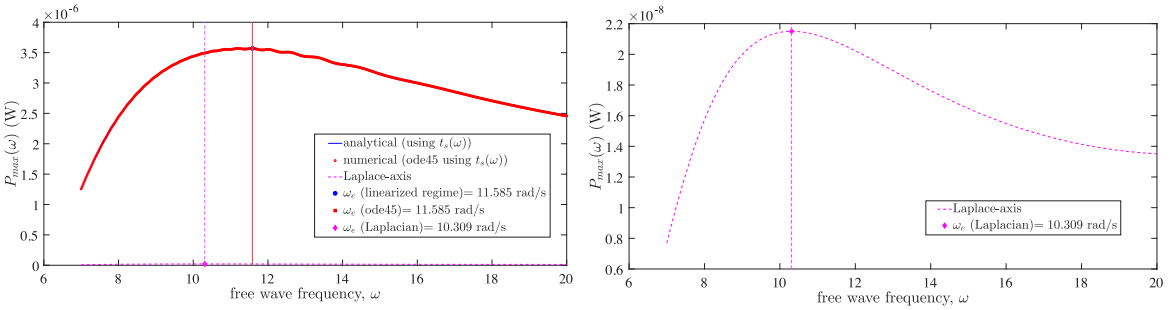

(a) Analytical time-domain estimate and Laplace prediction versus direct numerical integration

(b) Laplace-axis prediction (zoomed in)

Fig. 6. Comparison of analytical time-domain estimate, numerical integration, and Laplace-axis power prediction using $t_s(\omega)$ as calculated from (100), for the chosen parameter set, $t_s(\omega)$ varies from 9.69 to 10.14 s over the plotted frequency range, optimum frequency $\omega = \omega_e$ is marked at the peak power amplitude.

a smooth exponentially decaying function in time and an exponentially decaying function in time with initial transients/oscillatory components which die out eventually. Hence, a suitable time-domain approximation for the tip mass displacement $Y_n(t)$ from the stable equilibrium position at Y_s can be assumed to be of the form:

$$Y_n(t) \approx Ae^{-st} + Be^{\left(-\sigma \pm i\omega_d\right)t} \tag{86}$$

Now, once we have an idea about the approximate closed-form behavior of the tip mass Y_n in the time-domain, we use the concept of 'settling time' for Linear Time Invariant (LTI) systems to evaluate the time after which the transients finally settle on a smooth envelope. We can also make this suitable ansatz that the time after which the initial oscillatory transients die out in the displacement $Y_n(t)$ is close to the same time after which the initial transients die out in the voltage $V_n(t)$ and $V_n(t)$ grows along a smooth envelope from a negative value toward zero or in other words $|V_n(t)|$ decays along a smooth envelope from a positive value toward zero as shown in Fig. 4(b). Since we are interested in the harvested power which depends on $|V_n(t)|$, this seems to be an ansatz which is worthwhile.

Then, we go back to our dispersion relation in the linearized regime given by (42) and the closed-form definition posed for $\cos\mu = \cosh\beta$ in Section 7.1.2. So, in essence, defining our wavenumber dependent parameter $\cos\mu$ boils down to evaluating the $\cos^{-1}$ of an imaginary number in the form of $a + ib$, where a and b are real. In our case, we can explicitly write

$$a = 1 - \frac{M_t\omega^2 - k_{eff} - 2c_1 - 12c_2Y_s^2}{2k + r_a\omega^2}, b = -\frac{\Theta^2\omega R_l}{(2k + r_a\omega^2)(1 - \omega^2\tau^2)} \tag{87}$$

where $k_{eff} = \frac{EI\pi^4}{32L^3}$, $\tau = R_lC_p$ is the electrical time constant of the harvester. When $|a| < 1$, then $\cos^{-1}(z) = \cos^{-1}(a + ib)$ is analytic at $z = a$ and for small value of $|b|$, specifically for $|b| < 1 - |a|$, we can expand the function $\cos^{-1}(z)$ around $z = a$ in a Taylor series in terms of b by retaining up to cubic terms as:

$$\cos^{-1}(z) \approx \cos^{-1}(a + ib) = \cos^{-1}(a) - i\frac{b}{\sqrt{1 - a^2}} + \frac{ab^2}{2(1 - a^2)^{\frac{3}{2}}} + i\frac{(1 + 2a^2)b^3}{6(1 - a^2)^{\frac{5}{2}}} \tag{88}$$

Then, we can separate the imaginary part of $\cos^{-1}(a + ib)$ as:

$$Im\left(\cos^{-1}(a + ib)\right) \approx -\frac{b}{\sqrt{1 - a^2}} + \frac{(1 + 2a^2)b^3}{6(1 - a^2)^{\frac{5}{2}}} \tag{89}$$

Where we retain up to cubic terms in b. Evaluating the sgn function remains a trivial task because it boils down to evaluating the sign of a real function of real variables given by $sgn = \text{sgn}\left(1 - \frac{M_t\omega^2 - k_{eff} - 2c_1 - 12c_2Y_s^2}{2k + r_a\omega^2}\right)$. Then our real $\cos\mu$ takes the form:

$$\cos\mu(\omega) = \cosh\beta(\omega) \approx \cosh\left(sgn * \left| -\frac{b(\omega)}{\sqrt{1 - a(\omega)^2}} + \frac{(1 + 2a(\omega)^2)b(\omega)^3}{6(1 - a(\omega)^2)^{\frac{5}{2}}} \right| \right) \tag{90}$$

This provides a compact approximation for the real-valued attenuation parameter needed in the settling-time estimate.

7.3.1. Concept of 'settling time' adapted to the free-decay voltage

For each fixed free-wave frequency ω, the linearized electromechanical model defines a linear time-invariant (LTI) system, whose free response $V_n(t)$ can be written as a superposition of modal exponentials

$$V_n(t;\omega) = \sum_j A_j(\omega)\, e^{s_j(\omega)t} \tag{91}$$

where $\{s_j(\omega)\}$ are the poles (equivalently, eigenvalues) of the linearized system and the coefficients $A_j(\omega)$ depend on the initial conditions

In standard control theory for Linear Time Invariant (LTI) systems, if the dominant transient is governed by an underdamped complex-conjugate pair

$$s_{2,3}(\omega) = -\sigma(\omega) \pm i\,\omega_d(\omega) \tag{92}$$

Then the oscillatory envelope decays approximately as $e^{-\sigma(\omega)t}$, and the settling time to a prescribed tolerance ϵ is estimated by

$$t_s(\omega) \approx \frac{\ln(1/\epsilon)}{\sigma(\omega)} \tag{93}$$

Common choices for the tolerance are $\epsilon = 0.02$ (2% criterion) giving $t_s \approx 4/\sigma$ and $\epsilon = 0.01$ (1% criterion) giving $t_s \approx 4.6/\sigma$

In our free-decay setting, the final value of $V_n(t)$ is zero, and the practical meaning of 'transients have settled' is that the oscillatory components have decayed below a chosen tolerance so that $V_n(t)$ evolves along a smooth envelope. Accordingly, we define an ω-dependent transient-decay time as:

$$t_s(\omega) \approx \frac{\ln(1/\epsilon)}{\sigma_{\text{osc}}(\omega)} \tag{94}$$

where $\sigma_{\text{osc}}(\omega)$ is the decay rate associated with the oscillatory (complex-conjugate) pole pair of the system This choice targets the decay of oscillations rather than the slowest real pole, because the latter may control very long-time tail behavior without necessarily governing when the voltage envelope becomes visually smooth over one period.

7.3.2. Explicit parameter-level approximation for $\sigma_{\text{osc}}(\omega)$ and $t_s(\omega)$ and comparison with numerical results

From the Laplace-domain formulation in Section 7.2.1, the transient decay is governed by the roots of the characteristic denominator

$$\Delta(s;\omega) = \left(m_e(\omega)s^2 + K(\omega)\right)\left(C_p s + \frac{1}{R_l}\right) + \Theta^2 s \tag{95}$$

Expanding Δ yields a cubic polynomial

$$m_e(\omega)C_p\, s^3 + \frac{m_e(\omega)}{R_l}\, s^2 + \left(K(\omega)C_p + \Theta^2\right)s + \frac{K(\omega)}{R_l} = 0 \tag{96}$$

Introducing the electrical time constant and two convenient normalized parameters as done earlier in Section 7.1.1,

$$\tau = R_l C_p \qquad \omega_m^2(\omega) = \frac{K(\omega)}{m_e(\omega)} \qquad \kappa(\omega) = \frac{\Theta^2}{m_e(\omega)C_p}$$

the characteristic equation can be written as

$$s^3 + \frac{1}{\tau}s^2 + \left(\omega_m^2(\omega) + \kappa(\omega)\right)s + \frac{\omega_m^2(\omega)}{\tau} = 0 \tag{97}$$

In the common regime where the roots separate into one predominantly real slow pole and one underdamped complex-conjugate pair, a useful approximation for the slow real pole is obtained by balancing the last two terms in (97).

$$s_r(\omega) \approx -\frac{\omega_m^2(\omega)}{\omega_m^2(\omega) + \kappa(\omega)}\,\frac{1}{\tau}$$

Using the sum of roots relation for the cubic, the real part of the complex pair then satisfies, considering the fact that for stable bounded solution in time, the real part of the complex conjugate pair should be negative:

$$-2\,\sigma_{\text{osc}}(\omega) + s_r(\omega) \approx -\frac{1}{\tau} \implies 2\,\sigma_{\text{osc}}(\omega) \approx s_r(\omega) + \frac{1}{\tau} \implies \sigma_{\text{osc}}(\omega) \approx \frac{1}{2\tau}\,\frac{\kappa(\omega)}{\omega_m^2(\omega) + \kappa(\omega)} \tag{98}$$

Substituting back $\tau = R_l C_p$, $\omega_m^2 = K/m_e$, and $\kappa = \Theta^2/(m_e C_p)$ in (98) gives a particularly compact ratio

$$\frac{\kappa(\omega)}{\omega_m^2(\omega) + \kappa(\omega)} = \frac{\Theta^2}{K(\omega)C_p + \Theta^2}$$

Hence, an explicit decay-rate estimate is $\sigma_{\text{osc}}(\omega) \approx \frac{1}{2R_l C_p}\,\frac{\Theta^2}{K(\omega)C_p+\Theta^2}$ and the corresponding transient-decay time becomes:

$$t_s(\omega) \approx \frac{\ln(1/\epsilon)}{\sigma_{\text{osc}}(\omega)} \approx 2R_l C_p\,\frac{K(\omega)C_p + \Theta^2}{\Theta^2}\,\ln\!\left(\frac{1}{\epsilon}\right) \tag{99}$$

Taking the most common choice for the tolerance value as $\epsilon = 1\% = 0.01$ gives the final explicit expression for the optimum time $t_s(\omega)$ as:

$$t_s(\omega) = 9.2\,\tau\,\frac{K(\omega)C_p + \Theta^2}{\Theta^2} \tag{100}$$

In our dispersion-based parameterization, the effective stiffness and mass depend on the attenuation parameter $\beta(\omega)$ through

$$K(\omega) = 2k\left(1 - \cosh(\beta(\omega))\right) + k_{eff} + 2c_1 + 12c_2 Y_s^2 \qquad m_e(\omega) = M_t - r_a\left(1 - \cosh(\beta(\omega))\right)$$

where $\cosh\beta(\omega)$ is obtained from the approximate relation derived in (90). The expression derived in (100) provides an explicit, parameter-level approximation for $t_s(\omega)$ which we have defined as the settling time to extract the voltage to compute the maximum harvested power for a particular value of the frequency in Section 7.1.2 (Eq. (50).

As a check that our approximated procedure matches effectively with direct numerical time-domain (ode45) simulations, we use our approximate closed-form expression derived in (100) to evaluate the optimum settling time for an input value of free wave frequency set to $\omega = 8$, the same frequency value used to obtain the time-domain response $Y_n(t)$ and $V_n(t)$ in Fig. 4. Our closed-form expression gives a value for the optimum time t_s as:

$$t_s = 9.83338 \approx 10 \text{ seconds} \tag{101}$$

This value agrees quite well with the time taken for the tip mass displacement to settle to a smooth envelope as shown in Fig. 4(a). The analytical estimate is approximately 50% below the visually identified value of $t_s \approx 20$ used in Section 5, which is expected given the conservative nature of the visual approximation. Both values lie well within the 80 s simulation window in Fig. 4.

We can hence use this generalized closed-form expression for $t_s(\omega)$ to compute the maximum harvested power for each input frequency ω by using the analytical definition in (50). This closes the gap that remained in linking back the last remaining book-keeping parameter $t_s(\omega)$ to the inherent system design parameters. We have already done the same in 7.1.2 for the other two book-keeping parameters, which were ω and the time period of the cycle $T_d(\omega)$ over which we intend to average the maximum power in the post-transient regime after t_s.

In a special scenario of our periodic chain, with no permanent base magnets and inertial amplifiers, and the tip mass made of a non-magnetic material, the periodic model reduces to a simple linear piezoelastic chain. In that case, our settling-time analytical approximation in the linearized regime still remains valid for the coupled linear electromechanical system with similar qualitative time-domain behavior of tip mass and voltage. The wavenumber (or frequency) dependent stiffness will just reduce to $K(\omega) = 2k\left(1 - \cosh(\beta(\omega))\right) + k_{eff}$, and the effective mass m_e reduces to just $m_e = M_t$. β can be obtained from the dispersion relation (29) by putting $c_1 = c_2 = r_a = 0$. The same approximate formula obtained in (100) can then be applied as it is.

7.3.3. Applicability and limitations of the 'settling time' concept

The 'settling time' estimate is applicable for our case because, for each fixed ω, the linearized dynamics define an LTI system and the voltage response is a linear combination of modal exponentials whose decay rates are dictated by the poles $s_j(\omega)$ Consequently, a settling-time scale based on the dominant oscillatory decay rate $\sigma_{\text{osc}}(\omega)$ provides a principled approximation for the time at which the oscillatory transients become small and the voltage evolves along a smooth envelope

Two practical limitations should be noted:

- Firstly, sweeping ω produces a family of LTI systems because $\beta(\omega)$ (and hence $K(\omega)$ and $m_e(\omega)$) varies with ω, so the identity of the dominant pole pair may change across the sweep.
- Secondly, when the poles are not well separated (e.g. near repeated roots, near stability boundaries, or near singular electrical factors), a single exponential envelope approximation becomes less accurate and the settling time may be better estimated directly from the computed pole set $\{s_j(\omega)\}$ rather than from a closed-form approximation.

7.4. Comparison of theoretical power with numerical time-domain integration

We use same initial conditions for both the analytical and numerical methods for the tip mass i.e. $Y_n(0) = 0.01$, $\dot{Y}_n(0) = 0$ and zero initial voltage $V_n(0) = 0$ which comes quite obviously considering our primary goal which is to generate/build up voltage and hence power harvesting the energy from free wave motion through our system. The spring stiffness coefficient and the inertial amplifier mass are chosen as $k = 0.1k_{eff}$ and $m_a = 0.5M_t$. Other parameters are chosen as in Table 2.

Fig. 6 shows the comparison between the analytically and numerically obtained maximum steady state power's variation with the free wave frequency ω. The value of $t_s(\omega)$ as obtained from (100) is used for both the analytical formulation derived in Section 7.1.2 and time-domain simulations using ode45. To calculate power directly in the Laplace domain $P(\omega) = |V(i\omega)|^2/(2R_l)$, without using any time-constraint, the formulation derived in Section 7.2.1 has been employed.

The excellent agreement between the analytical time-domain curve and the ode45 results in Fig. 6(a) confirms that the proposed time-domain framework reproduces both the peak magnitude (3.569416×10^{-6} W) and the peak location (optimum frequency $\omega_e = 11.5852$ rad/s) when the same power-extraction rule i.e. one-period averaging over $T_d(\omega)$ after $t_s(\omega)$ as calculated/evaluated from (100) is enforced. In contrast, the Laplace-axis curve (zoomed in Fig. 6(b)) predicts a different optimum frequency $\omega_e = 10.3086$ rad/s (as calculated from (80)) and, in general, a different attainable peak level, which is 2.150071×10^{-8} W. This discrepancy reflects the limitation discussed in Section 7.2.2. Evaluating $V(s)$ on the imaginary axis implicitly treats the response as a purely harmonic steady-state frequency response, whereas the quantity plotted in the time domain is a windowed maximum power extracted from a free decay transient after the mechanical modes have sufficiently settled. Because this windowed criterion depends on decay rates (real parts of eigenvalues), modal interference, and the finite-time envelope evolution of $V_n(t)$, it is not fully captured by $s = i\omega$ alone. Consequently, the direct Laplace-axis formulation remains useful for rapid analytical magnitude estimates, settling time formulation and trend studies, but recovering an optimum frequency consistent with the deterministic time-domain metric requires reconstructing $V_n(t)$, e.g. via inverse Laplace/eigen-expansion and applying the same $t_s(\omega)$-based power criterion.

8. General strongly nonlinear regime

We now consider the piezomagnetoelastic periodic chain in its general nonlinear regime where the tip mass is allowed to undergo sufficiently large amplitudes of motion and hence the cubic term Y_n^3 becomes dominant. Since in our proposed periodic model, even in the strongly nonlinear regime, the nonlinearities are confined within a unit cell and the intercellular coupling springs are linear, we assume a Bloch-consistent harmonic approximation (Bhattacharyya & Adhikari., 2026; Narisetti, 2010) for the tip mass displacement in the regime of free wave propagation in the form:

$$Y_n(t) = \left(\sum_{m=1}^{M} A_m \cos\left[m(\mu.\mathbf{n} - \omega t)\right] + B_m \sin\left[m(\mu.\mathbf{n} - \omega t)\right] \right) \tag{102}$$

where $\mu.\mathbf{n} = \mu_1 n_1 + \mu_2 n_2$ is the inner product of the non-dimensional wavenumber vector with the directional vector of the general 2-D periodic lattice. M represents the number of harmonics considered. A_m and B_m are the unknown harmonic coefficients to be determined from the initial conditions. Since ours is a one-dimensional periodic system, $\mu.\mathbf{n} = \mu_1 n_1 + \mu_2 n_2$ simplifies to μn with n being the index of the repeating unit cell. Without loss of generality, we can choose the representative unit cell to be at $n = 0$, then the adjacent unit cells will have indices of -1 and $+1$. and μn reduces to $\pm\mu$.

We characterize free wave propagation when the tip mass is subject to a bi-stable magnetic potential function with two local minima and one local maxima. Choosing the distance between the magnets $d = 2d_h$, the vertical distance between the tip magnet's and base magnets' axis d_v and the field strength B_t at tip magnet's surface accordingly will result in a bi-stable magnetic potential well in terms of tip mass displacement Y_n corresponding to two stable and one unstable equilibrium position as discussed in Section 4.1 and associated values of the constant coefficients in the magnetic potential function. Henceforth, for generalization throughout the nonlinear analysis, we will represent these coefficients as $2c_1 = a_1$ and $4c_2 = a_2$. Rewriting (11) and taking the integer $j = 1$ without loss of generality gives the equation of motion in the general strongly nonlinear regime as:

$$\begin{aligned} M_t \ddot{Y}_n + k_{eff} Y_n + k\left(2Y_n - Y_{n-1} - Y_{n+1}\right) + a_1 Y_n + a_2 Y_n^3 \\ - \frac{m_a \cos^2\alpha}{2\sin^2\alpha}\left(2\ddot{Y}_n - \ddot{Y}_{n-1} - \ddot{Y}_{n+1}\right) - \Theta V_n = 0 \end{aligned} \tag{103}$$

8.1. Amplitude-dependent dispersion relation within a potential well

To characterize free wave motion within one of the two stable wells of the total potential of the tip mass, we first determine the static equilibrium from the simplest uniform branch as done previously for the linearized regime in Section 4.1. We now introduce the intrawell perturbation variable for the generalized strongly nonlinear regime as

$$Y_n(t) = Y_s + u_n(t) \tag{104}$$

Substituting (104) into (103) and equating to zero the collective terms responsible for satisfying the fixed point criteria gives

$$M_t \ddot{u}_n + K_t u_n + k\left(2u_n - u_{n-1} - u_{n+1}\right) + 3a_2 Y_s u_n^2 + a_2 u_n^3 - \frac{r_a}{2}\left(2\ddot{u}_n - \ddot{u}_{n-1} - \ddot{u}_{n+1}\right) - \Theta V_n = 0 \tag{105}$$

where

$$r_a = \frac{m_a \cos^2\alpha}{\sin^2\alpha} \tag{106}$$

To allow oscillations around a non-zero mean inside the potential well, we augment the harmonic expansion (102) with a zero harmonic and express the perturbation from the stable equilibrium position in the Bloch-consistent harmonic expansion form as:

$$u_n(t) = U_0 + \sum_{m=1}^{M} \left[A_m \cos m(\mu n - \omega t) + B_m \sin m(\mu n - \omega t)\right] \tag{107}$$

Restricting to the zero harmonic and the first harmonic for small-amplitude intrawell oscillations gives

$$u_n(t) \approx U_0 + A_1 \cos(\mu n - \omega t) + B_1 \sin(\mu n - \omega t) = U_0 + R\cos(\mu n - \omega t - \phi) \tag{108}$$

where

$$R = \sqrt{A_1^2 + B_1^2} \tag{109}$$

Using the first harmonic truncation with zero harmonic addition, the quadratic and cubic displacement terms in (105) are approximated by retaining only the constant and fundamental-harmonic components:

$$u_n^2(t) \approx \left(U_0^2 + \frac{R^2}{2}\right) + 2U_0 R\cos(\mu n - \omega t - \phi) \tag{110}$$

$$u_n^3(t) \approx \left(U_0^3 + \frac{3}{2}U_0 R^2\right) + \left(3U_0^2 R + \frac{3}{4}R^3\right)\cos(\mu n - \omega t - \phi) \tag{111}$$

The electrical equation (12) is linear in voltage $V_n(t)$. Therefore, the zero harmonic gives

$$V_0 = 0 \tag{112}$$

while the first harmonic satisfies

$$\hat{V}_1 = \frac{i\omega\Theta}{\frac{1}{R_l} - i\omega C_p}\,\hat{U}_1 \tag{113}$$

The zero harmonic component U_0 after substituting (108),(110),(111) in (105) yields the zero harmonic balance equation

$$K_t U_0 + 3a_2 Y_s\left(U_0^2 + \frac{R^2}{2}\right) + a_2\left(U_0^3 + \frac{3}{2}U_0 R^2\right) = 0 \tag{114}$$

The fundamental component gives

$$\left[K_t + 2k(1-\cos\mu) - \omega^2\left(M_t - r_a(1-\cos\mu)\right) - \frac{i\omega\Theta^2}{\frac{1}{R_l} - i\omega C_p} + 6a_2 Y_s U_0 + 3a_2 U_0^2 + \frac{3}{4}a_2 R^2\right]\hat{U}_1 = 0 \tag{115}$$

For a non-trivial first harmonic, $\hat{U}_1 \neq 0$, Eq. (115) gives the amplitude-dependent dispersion relation within the selected potential well:

$$\cos\mu = 1 - \frac{M_t\omega^2 - K_t - 6a_2 Y_s U_0 - 3a_2 U_0^2 - \frac{3}{4}a_2 R^2 + \frac{i\omega\Theta^2}{\frac{1}{R_l} - i\omega C_p}}{2k + r_a\omega^2} \tag{116}$$

This gives the amplitude-dependent dispersion relationship inside a static potential well in the general strongly nonlinear regime. It differs from the zero-mean relation by the appearance of the zero-harmonic correction U_0 and the equilibrium shift Y_s, both of which arise from the asymmetry of the local oscillation about the non-zero stable equilibrium.

For the representative unit cell, we can take $n = 0$ without loss of generality. Then, the initial conditions are imposed on the perturbation u_n as

$$u_n(0) = \epsilon, \qquad \dot{u}_n(0) = \dot{Y}_n(0) \tag{117}$$

where $\epsilon = Y_n(0) - Y_s$. From (108), the corresponding amplitude is

$$R = \sqrt{(\epsilon - U_0)^2 + \left(\frac{\dot{Y}_n(0)}{\omega}\right)^2} \tag{118}$$

If the initial velocity is zero, then

$$R = |\epsilon - U_0| \tag{119}$$

Small-amplitude approximation: If R is sufficiently small, then $U_0 = O(R^2)$. Neglecting U_0^2 and U_0^3 in (114) gives

$$U_0 \approx -\frac{3a_2 Y_s}{2K_t}R^2 \tag{120}$$

and substituting this in (116) and using the expression for the stable equilibrium point Y_s as obtained in (15) yields the reduced local approximation

$$\cos\mu \approx 1 - \frac{M_t\omega^2 - K_t + \frac{15}{4}a_2 R^2 + \frac{i\omega\Theta^2}{\frac{1}{R_l} - i\omega C_p}}{2k + r_a\omega^2} \tag{121}$$

This can be rationalized further to:

$$\cos\mu \approx 1 - \frac{\left(M_t\omega^2 - K_t + \frac{15}{4}a_2 R^2\right)\left(1 + \omega^2\tau_e^2\right) + i\omega\Theta^2 R_l\left(1 + i\omega\tau_e\right)}{\left(2k + r_a\omega^2\right)\left(1 + \omega^2\tau_e^2\right)}. \tag{122}$$

where $\tau_e = R_l C_p$ is the electrical time constant.

The role of the nonlinear terms can now be interpreted more clearly. In the small-amplitude limit about a stable equilibrium, the magnetic nonlinearity first appears through the tangent stiffness of the selected potential well, and therefore it primarily shifts the local dispersion relation, the effective resonance condition, and the frequency at which maximum harvesting occurs. However, in the finite-amplitude intrawell regime, the nonlinear terms do more than simply shift a linear resonance. The amplitude R and the zero-harmonic correction U_0 enter the dispersion relation explicitly, so the admissible free-wave branch becomes amplitude-dependent. In addition, the underlying double-well magnetic potential introduces multistability, with two stable equilibria separated by an unstable saddle. Thus, depending on the initial condition, the same physical unit cell can support distinct dynamical regimes such as small intrawell oscillations, larger amplitude intrawell motion with amplitude-dependent frequency content, and, for sufficiently large perturbations, interwell transitions. The present harvesting analysis focuses on the stable intrawell branch, where these nonlinear effects reshape the harvesting response into a broader near-optimal operating band without relying on unstable negative-stiffness motion.

8.2. Time-domain response and energy harvested in the strongly nonlinear regime

In the strongly nonlinear regime, we characterize the system response, i.e., tip mass displacement and voltage generated for intrawell oscillations of the tip mass within the potential well centered at $Y_n = +Y_s$.

We obtain the time-domain response via a continuation method to find the converged nonlinear dispersion branch $\mu(\omega)$ for a desired target value of ω. For small amplitudes within a local potential well, we use the dispersion relation obtained in (116). It is worthwhile to note here that assuming our nonlinear model described by ((105), (12)) even for small-amplitude oscillations in the vicinity of the stable equilibrium point $+Y_s$ will exhibit the same qualitative behavior as our linearized model described by ((22), (12)) will be erroneous, since $+Y_s$ is a center. In the vicinity of a center, we cannot make any prediction on the qualitative behavior of our nonlinear model based on the linearized model's dynamic response (Strogatz, 1994). Since our system is symmetric in the static equilibrium for the simplest uniform branch, it is reasonable to assume that considering the potential well centered at $Y_n = -Y_s$ will yield the same characteristics in terms of time-domain response and energy harvesting potential.

8.2.1. Small-amplitude intrawell oscillations about a stable center

To obtain the small-amplitude intrawell response in the general strongly nonlinear regime, we construct the nonlinear Bloch branch by continuation in the book-keeping parameter ω starting from a low-amplitude seed point within the same stable potential well. At each continuation step, the previously converged values of the zero-harmonic correction U_0 and the Bloch wavenumber μ are used as predictor values, and are then corrected by solving the zero-harmonic balance equation (114) together with the amplitude-dependent dispersion relation (116), while updating the oscillation amplitude R from the imposed initial perturbation about the equilibrium position at $+Y_s$. As an initial guess for the zero-harmonic component U_0, we use the small amplitude approximation in (120). This predictor–corrector procedure ensures that the solution remains on the same intrawell nonlinear branch, avoids spurious jumps to neighboring roots of the algebraic system, and provides a converged branch $\mu(\omega)$ which is then used in the direct time-domain integration of the governing equations ((105), (12)) for the representative unit cell.

We use the same purely evanescent Bloch wave approximation for the wavenumber μ as $\cos\mu = sgn * \cosh\beta$, where $\beta = |Im(\mu)|$ and the sgn function defined as $sgn = \text{sgn}(\cos\mu)$, where $\cos\mu$ is given by the amplitude-dependent dispersion relation in (122). Since for strictly intrawell oscillations, we do not want to enter the negative-stiffness region, we impose a feasibility constraint on the net wavenumber-dependent effective stiffness as $K(\mu) = K_t + 2k(1-\cos\mu) > 0$ for the general strongly nonlinear regime.

8.2.2. Time-domain response of tip mass displacement for intrawell oscillations and voltage generated

Fig. 7 shows the time-domain response and Poincare maps of the tip mass and voltage generated for the single harmonic dispersion relation in the strongly nonlinear regime (122) with a target value of free wave frequency $\omega = 20$ and spring stiffness and inertial amplifier mass chosen to be the same as in the linearized regime, i.e., $k = 0.1k_{eff}$, $m_a = 0.5M_t$. To generate the Poincare maps for our unforced system, we plot the points evaluated in the phase space $Y_n(t)$, $\dot{Y}_n(t)$ and $V_n(t)$, $\dot{V}_n(t)$ whenever time t is an integer multiple of $\frac{2\pi}{\omega_n}$, where

$$\omega_n = \sqrt{\frac{K(\mu)}{M_t - r_a(1-\cos\mu)}} \tag{123}$$

with $\cos\mu$ obtained from the dispersion relation in (122).

The tip mass still remains in the potential well at $Y_s = +0.0107$ for the chosen initial perturbation as is evident from Fig. 7(a) and the Poincare map in Fig. 7(c). The time-domain responses show similar behavior qualitatively with that in the linearized regime in Fig. 4 obtained with the same initial perturbation on the tip mass. Though the feasibility constraint to obtain stable transient oscillatory behavior has shifted the input free wave frequency value required from $\omega = 8$ to $\omega = 20$. Later, we will see what this implies in terms of system design parameters in terms of enhanced energy harvesting potential when compared to the linearized model.

Once we get an idea of the dynamic behavior related to intrawell oscillations in the strongly nonlinear regime, we evaluate the maximum power harvested in the steady state as a function of the free wave frequency, considered again as a book-keeping parameter as of now. Since in the general strongly nonlinear regime even for small-amplitude intrawell oscillations, we cannot pose any reduced eigenvalue problem, our previously introduced concept of settling time and hence optimal power constraint criterion cannot be set up in a closed-form in terms of the book-keeping parameter (more colloquially called free wave frequency). Hence, we use the settling time formula derived in (100) in the linearized regime to evaluate the maximum steady-state power harvested. We choose the same initial perturbation on the tip mass from the stable equilibrium position at $Y_s = 0.0107$ to generate intrawell oscillations in the strongly nonlinear regime as was used for the linearized regime in Fig. 4(a) and in Fig. 7(a) for the nonlinear regime, i.e. $u_n(0) = 0.01 \implies Y_n(0) = Y_s + u_n(0) = 0.0207,\ \dot{Y}_n(0) = \dot{u}_n(0) = 0$.

8.2.3. Enhanced energy harvesting potential in terms of design implications

Fig. 8(a) shows that, once the intrawell nonlinear branch is evaluated under the admissibility constraints of bounded effective mass and positive effective stiffness, the harvested power no longer exhibits the narrow resonant-type optimum characteristic of the linearized baseline, but instead rises from the low-frequency end of the admissible branch and then approaches a broad quasi-saturated plateau over the remainder of the feasible frequency range. By contrast, Fig. 8(b) shows that, for the same structural choice $k = k_{eff}$ and $m_a = 0.1M_t$, the linearized intrawell response attains a distinct optimum at $\omega_e = 13.695$ and then decreases as

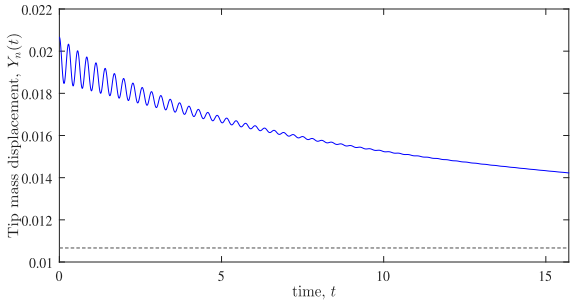

(a) Tip mass displacement $Y_n(t)$, the horizontal dashed line showing the stable equilibrium position $+Y_s$

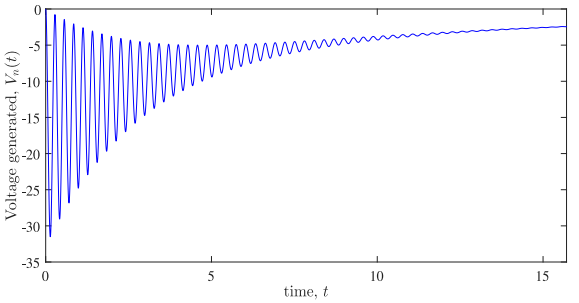

(b) Voltage generated $V_n(t)$

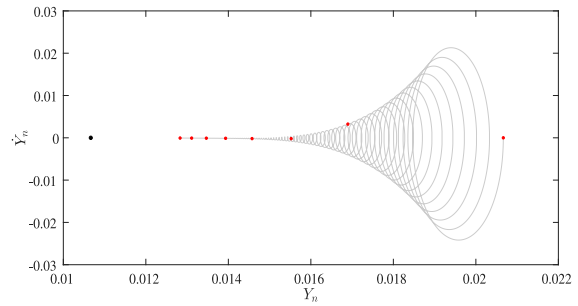

(c) Phase portrait of tip mass with the Poincare points, the black dot showing the stable equilibrium point $\left(Y_n(0), \dot{Y}_n(0)\right) = (+Y_s, 0)$

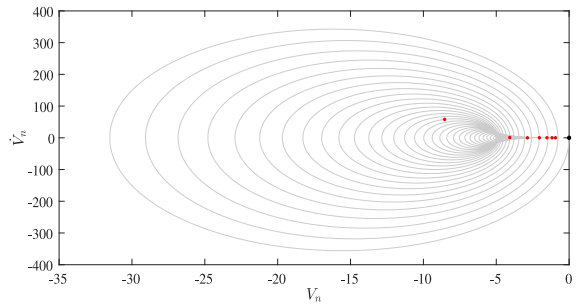

(d) Phase portrait of generated voltage with the Poincare points, the black dot showing the initial voltage $\left(V_n(0), \dot{V}_n(0)\right) = (0, 0)$

Fig. 7. Time-domain responses and phase portraits showing the tip mass displacement $Y_n(t)$ and voltage generated for intrawell oscillations in the strongly nonlinear regime $V_n(t)$ for a representative nth unit cell, for an initial perturbation on the tip mass as $Y_n(0) = 0.01, \dot{Y}_n(0) = 0$ from the stable equilibrium position at $Y_s = +0.0107$, $k = 0.1k_{eff}$, $m_a = 0.5M_t$, and with values of system parameters chosen as in Table 2.

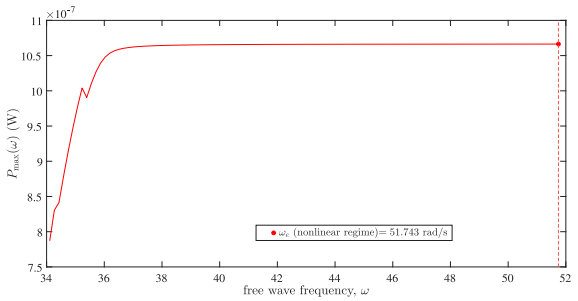

(a) Power harvested in the general strongly nonlinear regime ($k = k_{eff}$, $m_a = 0.1M_t$)

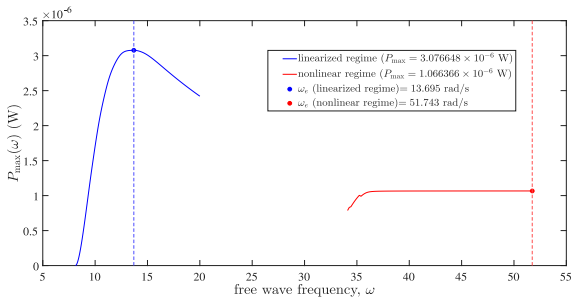

(b) Comparison between power harvested in the linearized and nonlinear regimes ($k = k_{eff}$, $m_a = 0.1M_t$)

Fig. 8. Comparison between power harvested in the general strongly nonlinear regime for intrawell oscillations within the stable potential well at $Y_n = +Y_s$ and power harvested in the linearized regime for the same small initial perturbation around the stable equilibrium point at $Y_n = +Y_s$.

ω is increased further. The strongly nonlinear regime therefore transforms the response from a sharply tuned operating point into a much wider near-optimal operating band while still maintaining a comparable maximum power magnitude. As it can be seen from the comparison in Fig. 8(b), the maximum power harvested for intrawell oscillations in the nonlinear regime is 1.07×10^{-6} W, while the maximum power harvested in the linearized regime is 3.08×10^{-6} W. In the context of enhanced vibration energy harvesting, this is a significant outcome because it indicates that the nonlinear piezomagnetoelastic chain can sustain almost constant maximum harvested power, comparable in magnitude to the linearized regime's power, over a substantially broader range of free-wave frequencies, rather than only in the immediate neighborhood of one isolated optimum.

In the present implementation, the post-transient extraction window used for the nonlinear intrawell branch is anchored to the linearized baseline through the settling-time estimate developed earlier. Specifically, we take a constant value $t_s = 10.015$, obtained

from (100) by evaluating the linearized framework at the optimum frequency $\omega = 13.695$ corresponding to the peak power in Fig. 8(b). In this sense, the linearized intrawell model provides the reference settling-time scale with which the general nonlinear response is evaluated. The resulting plateau in Fig. 8(a) should therefore not be interpreted as an artifact of premature power extraction, but rather as a genuine consequence of the strongly nonlinear branch structure. Equally importantly, this broad nonlinear operating window is obtained while satisfying all admissibility conditions imposed on the reduced branch, so that the response remains inside the selected potential well and does not enter the effective negative-stiffness regime. The broadened high-power band is thus realized without relying on inverted-stiffness dynamics or unbounded growth, and remains fully consistent with passive energy harvesting from stable intrawell oscillations.

From a design perspective, the nonlinear plateau admits a direct inverse-map interpretation. The free-wave frequency ω remains a book-keeping parameter, but it is one that is determined implicitly by the structural, inertial, magnetic, and electrical properties of the chain through the corresponding dispersion relation. Consequently, the much wider admissible frequency interval in Fig. 8(b) translates directly into a wider set of realizable system-parameter combinations that can deliver essentially saturated harvested power at comparable magnitudes with the linearized regime. This is especially important in the present case because the broadened nonlinear operating regime is obtained simultaneously with an increased/improved stiffness-to-weight ratio of the unit cell, achieved here by increasing the spring stiffness from $k = 0.1k_{eff}$ to $k = k_{eff}$ while reducing the inertial amplifier mass from $m_a = 0.5M_t$ to $m_a = 0.1M_t$. Such a shift toward higher stiffness and lower auxiliary inertia is always desirable in real structural design, since it reduces inertial penalty while preserving a wide high-performance harvesting window. At the same time, the nonlinearities shift the admissible operating range to higher values of the book-keeping frequency when compared to the linearized baseline, so that the ω-axis itself serves as an inverse design map for selecting improved ranges of system parameters for which high harvested power, intrawell stability, and positive effective stiffness are achieved simultaneously.

9. Concluding remarks and future work

This work has proposed an inertially amplified nonlinear piezomagnetoelastic chain as a physically realizable framework for harvesting energy from transient free waves, rather than from a prescribed sustained external excitation. Starting from a dissipative bi-stable unit cell, we showed that electromechanical coupling fundamentally alters the phase space structure of the isolated element and turns it into an energy converting building block for a periodic medium capable of attenuation and distributed electrical extraction. On this basis, a reduced electromechanical model was developed for the chain and analyzed in both the linearized intrawell and strongly nonlinear intrawell regimes.

In the linearized regime, the combination of Bloch reduction with a settling-time-aware power metric provided a predictive analytical framework for identifying the maximum steady-state harvested power and the associated free-wave operating frequency directly from the coupled structural, magnetic, inertial, and electrical parameters, with validation against numerical time-domain simulations. In the strongly nonlinear regime, the amplitude-dependent dispersion analysis and time-domain evaluation revealed that magnetic bi-stability and inertial amplification do not simply increase an isolated harvesting peak, but instead, they transform a sharply tuned linear operating point into a broad quasi-saturated band of near optimal performance over a much wider free wave frequency interval. Importantly, this enhancement is achieved within stable intrawell oscillations, without relying on negative-stiffness induced divergence, and is accompanied by an improved stiffness-to-weight ratio through stiffer coupling and lower auxiliary inertia.

In this sense, the paper fills the gap identified in existing literature by unifying nonlinear bi-stability, piezoelectric transduction, transient free wave motion, and inertial amplification within a single analytical and computational framework. More broadly, the results show that free wave propagation in nonlinear periodic electromechanical media can be treated not merely as a transient phenomenon, but as a deliberate design mechanism for robust and broadband energy harvesting.

Key novel features of this work include:

- Development of a nonlinear inertially amplified piezomagnetoelastic chain specifically for energy harvesting from transient free-wave motion generated solely by initial conditions, without requiring sustained external forcing.
- Establishment of a dissipative bi-stable unit-cell interpretation showing that electromechanical coupling converts the isolated element into a building block for distributed attenuation and spatially extended electrical extraction in the periodic chain.
- Formulation of a Bloch-based analytical framework, complemented by a closed-form settling-time criterion, to predict the maximum steady-state harvested power and the associated free-wave operating frequency directly from the coupled system parameters.
- Extension of the analysis to the strongly nonlinear regime through an amplitude-dependent dispersion relation and time-domain power evaluation.
- Demonstration that the strongly nonlinear regime broadens the harvesting response into a wide quasi-saturated near optimal operating band, rather than merely increasing a single-frequency peak.
- Identification of a practically attractive nonlinear design regime that preserves stable intrawell motion, avoids negative-stiffness induced divergence, and improves the stiffness-to-weight ratio through stiffer coupling and lower auxiliary inertia.

The present study has some limitations that define the scope of the conclusions. First, the main analytical framework is developed for a one-dimensional periodic chain and focuses primarily on intrawell dynamics around stable equilibria. Therefore, large-amplitude interwell transitions, possible chaotic responses, and strongly localized nonlinear waveforms are not treated in the

present work. Second, the electromechanical harvesting circuit is represented through a resistive load, which allows the role of the structural and inertial parameters to be isolated clearly, but does not include more advanced interface circuits. Third, although the analytical predictions are validated using numerical time-domain simulations, experimental realization, manufacturing tolerances, and parameter uncertainty remain outside the present scope. These limitations do not reduce the main contribution of the work. Rather, they identify the assumptions under which the proposed free-wave harvesting framework is presently established. Future work can therefore proceed in several directions. One of them is the investigation of large-amplitude interwell oscillations, for which bi-stable periodic chains may support localized soliton-like wavefronts, and nonlinear energy transport mechanisms. In addition, future studies may consider finite-chain boundary effects, parameter sensitivity, and experimental prototype validation to assess the robustness of the predicted broadband harvesting response. Finally, the integration of more advanced electrical interfaces, such as inductive, synchronized-switching, or adaptive impedance circuits, may further improve the conversion efficiency and extend the practical operating range of the proposed nonlinear electromechanical metamaterial.

CRediT authorship contribution statement

A. Bhattacharyya: Writing – review & editing, Writing – original draft, Visualization, Validation, Supervision, Software, Resources, Project administration, Methodology, Investigation, Formal analysis, Data curation, Conceptualization. **S. Adhikari:** Writing – review & editing, Visualization, Validation, Supervision, Software, Resources, Project administration, Methodology, Investigation, Funding acquisition, Formal analysis, Data curation, Conceptualization.

Declaration of competing interest

The authors declare that they have no known competing financial interests or personal relationships that could have appeared to influence the work reported in this paper.

Acknowledgment

This work was supported by UofG internal grant 30301020/201712-01.

Appendix A. Supplementary data

See Supplementary material for band structure and harvested power's variation with system parameters in the linearized regime. Supplementary material related to this article can be found online at https://doi.org/10.1016/j.ijengsci.2026.104573.

Data availability

Data will be made available on request.

References

Anton, S. R., & Sodano, H. A. (2007). A review of power harvesting using piezoelectric materials (2003–2006). *Smart Materials and Structures*, *16*(3), R1–R21.

Aravind Kumar, K., Ali, S. F., & Arockiarajan., A. (2015). Piezomagnetoelastic broadband energy harvester: Nonlinear modeling and characterization. *The European Physical Journal Special Topics*, *224*(14), 2803–2822.

Bhattacharyya, A., & Adhikari., S. (2026). Bandgap manipulation through a bi-stable inertially amplified strongly nonlinear periodic chain. *International Journal of Non-Linear Mechanics*, *187*, Article 105364.

Cao, Y., Huang, H., & He, W. (2020). Energy harvesting characteristics of preloaded piezoelectric beams. *Journal of Physics D (Applied Physics)*, *53*, Article 095501.

Carrara, M., Cacan, M. R., Leamy, M. J., Ruzzene, M., & Erturk, A. (2012). Dramatic enhancement of structure-borne wave energy harvesting using an elliptical acoustic mirror. *Applied Physics Letters*, *100*, Article 204105.

Carrara, M., Cacan, M. R., Toussaint, J., Leamy, M. J., Ruzzene, M., & Erturk, A. (2013). Metamaterial-inspired structures and concepts for elastoacoustic wave energy harvesting. *Smart Materials and Structures*, *22*, Article 065004.

Chaplain, G. J., De Ponti, J. M., Aguzzi, G., Colombi, A., & Craster, R. V. (2020). Topological rainbow trapping for elastic energy harvesting in graded Su–Schrieffer–Heeger systems. *Physical Review Applied*, *14*, Article 054035.

Cottone, F., Vocca, H., & Gammaitoni, L. (2009). Nonlinear energy harvesting. *Physical Review Letters*, *102*, Article 080601.

Daqaq, M. F., Masana, R., Erturk, A., & Quinn, D. D. (2014). On the role of nonlinearities in vibratory energy harvesting: A critical review and discussion. *Applied Mechanics Reviews*, *66*(4), Article 040801.

Erturk, A., & Inman, D. J. (2011). *Piezoelectric energy harvesting*. Wiley.

Esmailzadeh, E., & Nakhaie-Jazar., G. (1998). Periodic behavior of a cantilever beam with end mass subjected to harmonic base excitation. *International Journal of Non-Linear Mechanics*, *33*(4), 567–577.

Friswell, M., Ali, S. F., Bilgen, O., Adhikari, S., Lees, A. W., & Litak., G. (2012). Non-linear piezoelectric vibration energy harvesting from a vertical cantilever beam with tip mass. *Journal of Intelligent Material Systems and Structures*, *23*(13), 1505–1521.

Geng, Q., Wang, T., Wu, L., & Li, Y. (2021). Defect coupling behavior and flexural wave energy harvesting of phononic crystal beams with double defects in thermal environments. *Journal of Physics D (Applied Physics)*, *54*, Article 225501.

Gonella, S., To, A. C., & Liu, W. K. (2009). Interplay between phononic bandgaps and piezoelectric microstructures for energy harvesting. *Journal of the Mechanics and Physics of Solids*, *57*(3), 621–633.

Harne, R. L., & Wang, K.-W. (2013). A review of the recent research on vibration energy harvesting via bistable systems. *Smart Materials and Structures*, *22*(2), Article 023001.

Hussein, M. I., Leamy, M. J., & Ruzzene, M. (2014). Dynamics of phononic materials and structures: historical origins, recent progress and future outlook. *Applied Mechanics Reviews*, *66*(4), Article 040802.

Hwang, M., & Arrieta, A. F. (2022). Topological wave energy harvesting in bistable lattices. *Smart Materials and Structures*, *31*, Article 015021.

Kim, P., & Seok, J. (2014). A multi-stable energy harvester: dynamic modeling and bifurcation analysis. *Journal of Sound and Vibration*, *333*, 5525–5547.

Kushwaha, M. S., Halevi, P., Dobrzynski, L., & Djafari-Rouhani, B. (1993). Acoustic band structure of periodic elastic composites. *Physical Review Letters*, *71*(13), 2022–2025.

Lin, R., Hou, L., Chen, Y., Jin, Y., Saeed, N., & Chen, Y. (2023). A novel adaptive harmonic balance method with an asymptotic harmonic selection. *Applied Mathematics and Mechanics*, *44*(11), 1887–1910.

Lin, Z., & Tol, S. (2021). Elastic metasurfaces for full wavefront control and low-frequency energy harvesting. *Journal of Vibration and Acoustics*, *143*, Article 061005.

Lv, H., Tian, X., Wang, M. Y., & Li, D. (2013). Vibration energy harvesting using a phononic crystal with point defect states. *Applied Physics Letters*, *102*, Article 034103.

Meng, Q., Hou, L., Lin, R., Chen, Y., Saeed, N. A., Fouly, A., & Awwad, E. (2025). On a quasi-zero stiffness vibration isolator with multiple zero stiffness points for mass load deviation. *Applied Mathematical Modelling*, *145*, Article 116112.

Meng, Q., Hou, L., Wang, A., Lin, R., Li, Z., Zhong, S., Chen, Y., Saeed, N. A., Mohamed, A., & Awwad, E. (2025). Subharmonic response suppression of a quasi-zero stiffness system. *Journal of Sound and Vibration*, *594*, Article 118674.

Mikoshiba, K., Manimala, J. M., & Sun, C. T. (2013). Energy harvesting using an array of multifunctional resonators. *Journal of Intelligent Material Systems and Structures*, *24*(2), 168–179.

Moon, F. C., & Holmes, P. J. (1979). A magnetoelastic strange attractor. *Journal of Sound and Vibration*, *65*(2), 275–296.

Morel, A., Pillonnet, G., Gasnier, P., Lefeuvre, E., & Badel, A. (2018). Frequency tuning of piezoelectric energy harvesters thanks to a short-circuit synchronous electric charge extraction. *Smart Materials and Structures*, *28*, Article 025009.

Mosquera-Sánchez, J. A., & Jr., C. D. M. (2021). Dynamics and wave propagation in nonlinear piezoelectric metastructures. *Nonlinear Dynamics*, *105*(4), 2995–3023.

Nadkarni, N., Daraio, C., & Kochmann, D. M. (2014). Dynamics of periodic mechanical structures containing bistable elastic elements: From elastic to solitary wave propagation. *Physical Review E*, *90*(2), Article 023204.

Narisetti, R. K. (2010). *Wave propagation in nonlinear periodic structures*. Georgia Institute of Technology.

Oudich, M., & Li, Y. (2017). Tunable sub-wavelength acoustic energy harvesting with a metamaterial plate. *Journal of Physics D (Applied Physics)*, *50*, Article 315104.

Raney, J. R., Nadkarni, N., Daraio, C., Kochmann, D. M., Lewis, J. A., & Bertoldi, K. (2016). Stable propagation of mechanical signals in soft media using stored elastic energy. *Proceedings of the National Academy of Sciences*, *113*(35), 9722–9727.

Saeed, N. A., Ellabban, Y., Hou, L., Moatimid, G., Zhong, S., & Duraihem, F. Z. (2025). Nonlinear dynamics of a bio-inspired 2-DOF low-frequency X-shaped vibration isolator with m-to-n layers driven harmonically under simultaneous primary and 1: 1 internal resonances. *Chaos, Solitons & Fractals*, *190*, Article 115786.

Saeed, N., Ellabban, Y., Hou, L., Yi, H., Zhong, S., Duraihem, F., & Omara, O. (2025). Nonlinear vibration of quasi-zero stiffness structure with piezoelectric harvester and RL-load: intra-well and inter-well oscillation modes under 1: 1 internal resonance. *Applied Mathematics and Mechanics*, *46*(8), 1451–1474.

Saeed, N. A., Ellabban, Y., Hou, L., Zhong, S., & Duraihem, F. Z. (2025). Geometric nonlinear dynamics of a quasi-zero stiffness isolator integrated with an energy harvester: monostable, perfect zero-linear stiffness, and bistable oscillation modes. *Chaos, Solitons & Fractals*, *199*, Article 116633.

Saeed, N. A., Ellabban, Y., Moatimid, G., Hou, L., & Mohamed, A. (2024). Nonlinear interactions of an n-layer X-shape low-frequency vibration isolator equipped with a nonlinear vibration absorber at 1: 1 internal resonance: analytical and numerical investigations. *Physica Scripta*, *99*(10), Article 105207.

Saeed, N., Hou, L., Yi, H., Shukur, A., Alamry, S., & El-Shourbagy, S. (2026). On a broadband vibration isolator with tunable stiffness: from quasi-zero-stiffness to zero-stiffness behavior. *Applied Mathematics and Mechanics*, *47*(2), 255–282.

Scarselli, G., Nicassio, F., Pinto, F., Ciampa, F., Iervolino, O., & Meo, M. (2016). A novel bistable energy harvesting concept. *Smart Materials and Structures*, *25*, Article 055001.

Stephen, N. G. (2006). On energy harvesting from ambient vibration. *Journal of Sound and Vibration*, *293*, 409–425.

Strogatz, S. H. (1994). *Nonlinear dynamics and chaos*. Perseus Books Publishing.

Sugino, C., & Erturk, A. (2018). Analysis of multifunctional piezoelectric metastructures for low-frequency bandgap formation and energy harvesting. *Journal of Physics D (Applied Physics)*, *51*, Article 215103.

Wei, C., & Jing, X. (2017). A comprehensive review on vibration energy harvesting: modelling and realization. *Renewable and Sustainable Energy Reviews*, *74*, 1–18.

Williams, C. B., & Yates, R. B. (1996). Analysis of a micro-electric generator for microsystems. *Sensors and Actuators A: Physical*, *52*, 8–11.

Xiong, L., Tang, L., Liu, K., & Mace, B. R. (2018). Broadband piezoelectric vibration energy harvesting using a nonlinear energy sink. *Journal of Physics D (Applied Physics)*, *51*, Article 185502.

Yilmaz, C., Hulbert, G. M., & Kikuchi, N. (2007). Phononic band gaps induced by inertial amplification in periodic media. *Physical Review B*, *76*, Article 054309.